Research article

NMR IN BIOMEDICINE

Received: 31 October 2014, Revised: 28 January 2015, Accepted: 2 March 2015, Published online in Wiley Online Library: 27 April 2015

(wileyonlinelibrary.com) DOI: 10.1002/nbm.3294

Mapping human brain capillary water lifetime: high-resolution metabolic neuroimaging

William D. Rooney[a,b,c,d]*, Xin Li[a,b], Manoj K. Sammi[a,b],
Dennis N. Bourdette[d], Edward A. Neuwelt[e] and Charles S. Springer Jr[a,b,c]*

Shutter-speed analysis of dynamic-contrast-agent (CA)-enhanced normal, multiple sclerosis (MS), and glioblastoma (GBM) human brain data gives the mean capillary water molecule lifetime (τ_b) and blood volume fraction (v_b; capillary density–volume product ($\rho^{\dagger}V$)) in a high-resolution $^{1}H_2O$ MRI voxel (40 μL) or ROI. The *equilibrium* water extravasation rate constant, k_{po} (τ_b^{-1}), averages 3.2 and 2.9 s^{-1} in resting-state normal white matter (NWM) and gray matter (NGM), respectively ($n = 6$). The results (italicized) lead to three major conclusions. (A) k_{po} differences are dominated by capillary water permeability ($P_W^{\dagger}$), not size, differences. *NWM and NGM voxel k_{po} and v_b values are independent. Quantitative analyses of concomitant population-averaged k_{po}, v_b variations in normal and normal-appearing MS brain ROIs confirm $P_W^{\dagger}$ dominance.* (B) $P_W^{\dagger}$ is dominated (>95%) by a trans(endothelial)cellular pathway, not the $P_{CA}^{\dagger}$ paracellular route. *In MS lesions and GBM tumors, $P_{CA}^{\dagger}$ increases but $P_W^{\dagger}$ decreases.* (C) k_{po} tracks steady-state ATP production/consumption flux per capillary. *In normal, MS, and GBM brain, regional k_{po} correlates with literature MRSI ATP (positively) and Na^+ (negatively) tissue concentrations. This suggests that the $P_W^{\dagger}$ pathway is metabolically active. Excellent agreement of the relative NGM/NWM $k_{po}v_b$ product ratio with the literature ^{31}PMRSI-MT CMR_{oxphos} ratio confirms the flux property.* We have previously shown that the *cellular* water molecule efflux rate constant (k_{io}) is proportional to plasma membrane P-type ATPase turnover, likely due to active transmembrane water cycling. With synaptic proximities and synergistic metabolic cooperativities, polar brain endothelial, neuroglial, and neuronal cells form “gliovascular units.” We hypothesize that a chain of water cycling processes transmits brain metabolic activity to k_{po}, letting it report neurogliovascular unit Na^+,K^+-ATPase activity. Cerebral k_{po} maps represent metabolic (functional) neuroimages. The NGM 2.9 s^{-1} k_{po} means an *equilibrium* unidirectional water efflux of ~10^{15} H_2O molecules s^{-1} per capillary (in 1 μL tissue): consistent with the known ATP consumption rate and water co-transporting membrane symporter stoichiometries. © 2015 The Authors *NMR in Biomedicine* Published by John Wiley & Sons Ltd.

Keywords: high resolution; MRI; brain; metabolism; Na^+,K^+ pump; activity

INTRODUCTION

Every eukaryotic cell has a plasma membrane P-type ATPase ion pump; for animals, this is Na^+,K^+-ATPase (NKA) (1,2). Since its activity maintains the transmural K^+ and Na^+ gradients and thus, respectively, the membrane potential and secondary active transport, NKA is vital for life. The normal “forward” reaction is the following, where the i and o subscripts indicate intra- and extra-cellular, respectively.

$$ATP_i + 2\,K_o^{+} + 3\,Na_i^{+} \xrightarrow{NKA} ADP_i + P_i + 2\,K_i^{+} + 3\,Na_o^{+}$$

---

* *Correspondence to: W. D. Rooney, Charles S. Springer Jr, Advanced Imaging Research Center, Oregon Health and Science University, Portland, OR, USA. E-mail: rooneyw@ohsu.edu; springer@ohsu.edu*

a *W. D. Rooney, X. Li, M. K. Sammi, C. S. Springer Jr*
Advanced Imaging Research Center, Oregon Health and Science University, Portland, OR, USA

b *W. D. Rooney, X. Li, M. K. Sammi, C. S. Springer Jr*
W. M. Keck Foundation High-Field MRI Laboratory, Oregon Health and Science University, Portland, OR, USA

c *W. D. Rooney, C. S. Springer Jr*
Knight Cardiovascular Institute, Oregon Health and Science University, Portland, OR, USA

d *W. D. Rooney, D. N. Bourdette*
Department of Neurology, Oregon Health and Science University, Portland, OR, USA

e *E. A. Neuwelt*
Blood-Brain Barrier Program, Oregon Health and Science University, Portland, OR, USA

Abbreviations used: *ADP, adenosine diphosphate; ASL, arterial spin labeling; ATP, adenosine triphosphate; CA, contrast agent; CBV, cerebral blood volume; CESL/CEST, chemical exchange spin lock/saturation transfer; CMR_{oxphos}, cerebral metabolic rate of ATP synthesis from oxidative phosphorylation; DCE-MRI, dynamic-contrast-enhanced magnetic resonance imaging; F, cerebral blood flow (CBF); FDG, fluorodeoxyglucose; Fe-tol, ferumoxytol (Feraheme); FOV, field of view; FXL, fast-exchange limit; FXR, fast-exchange regime; GBM, glioblastoma multiforme; GBM-NA, GBM normal appearing; GdHPDO3A, gadoteridol (ProHance); GM, gray matter; HP, hyperpolarized; IR, inversion recovery; MR_{glc}, metabolic rate of glucose (consumption); MRSI, magnetic resonance spectroscopic imaging; MS, multiple sclerosis; MS-NA, MS normal appearing; MT, magnetization transfer; NAGM, normal-appearing gray matter; NAWM, normal-appearing white matter; NGM, normal GM; NKA, Na^+,K^+-ATPase; NWM, normal WM; PCr, phosphocreatine; PET, positron emission tomography; P_i, inorganic phosphate (PO_4^{3-}); ROI, region of interest; RRMS, relapsing–remitting MS; SPECT, single photon emission computed tomography; SSP, shutter-speed paradigm; SXR, slow-exchange regime; TI, inversion time; TP, tracer paradigm; TSC, tissue sodium concentration; WEI, water exchange index; WM, white matter; 2SX, two-site exchange.*

Even in homeostasis, the NKA pump experiences continual turnover (there are return pathways). It has been estimated that it consumes over 50% of brain adenosine triphosphate (ATP) (3). Methods for measuring NKA activity have been adapted to the experimental sample. For solubilized, purified enzyme or tissue homogenate preparations, spectrophotometric (4) or radiolabeled (^{32}P) (5) ATP hydrolysis rate assays suffice. For intact cells in culture or in tissue preparations, voltage clamp current, ion-selective (Na^+/K^+) microelectrode response, radioisotope ($^{22}Na^+/^{24}Na^+/^{42}K^+/^{86}Rb^+$) uptake/release (6–9), or $^{23}Na^+/^{87}Rb^+$ MRS (10,11) methods measure NKA-driven transmembrane ion transport kinetics. Phospholipid vesicles reconstituted with purified NKA allow measurement of both ATP hydrolysis and ion transport kinetics (5).

Each of these methods is best suited to macroscopically homogeneous samples. None are particularly appropriate for normally heterogeneous tissue, since there is no spatial encoding. Furthermore, many of these methods directly measure only *net* NKA activity, not homeostatic *turnover*. The radioisotope approach has been generally abandoned for about 20 years; deemed too problematic for even tissue preparations (12). As far as we are aware, NKA turnover has never been measured, let alone mapped, in a living animal or human subject. Doing so would provide a very fundamental view of ongoing metabolism, a new form of metabolic imaging. Since metabolic thermodynamics and kinetics have no necessary relationship (important example below), it is imperative to distinguish these aspects in imaging.

Mapping metabolic thermodynamics

Restricting ourselves essentially to human studies, so far metabolic imaging has been mostly accomplished by positron emission tomography (PET) (13) and magnetic resonance spectroscopic imaging (MRSI) (14,15), with some single photon emission computed tomography (SPECT) (16). Very often, this is mapping of metabolic molecule tissue concentrations ("levels") – the thermodynamic dimension of metabolism. For example, ^{31}PMRSI gives the distribution of high-energy phosphate brain levels (17). Such data could be used to estimate the cerebral distribution of the free energy for ATP hydrolysis (10,18). ^{23}NaMRSI maps tissue sodium concentration (TSC) (19). If a TSC increase reflects an intracellular sodium, Na_i^+, increase, it signifies a decrease in the transcytolemmal sodium electrochemical potential gradient (19). ^{1}HMRSI can map the lactate, N-acetylaspartate, and choline-containing (20) metabolites. Other thermodynamic aspects assessed include H_3O^+ (pH), O_2 (diminished in hypoxia), and redox level distributions (21). Newer metabo-CESL/CEST (chemical exchange spin lock/saturation transfer) methods use RF pulses to detect metabolite (creatine (22), glucose (23,24)) resonances via the ^1H_2O MR signal. Though receptors are not metabolites, PET and SPECT can be used to map their tissue concentrations (25,26). For example, the [^{11}C]cocaine tracer was used to determine the dopamine transporter concentration, 700 nM, in the abuser *striatum* (25). Receptors very often catalyze, or trigger by signaling, metabolic reactions.

Mapping metabolic kinetics

For all the power of thermodynamics, kinetic metabolic aspects – enzyme-catalyzed fluxes (rates) – can be more informative. With PET and hyperpolarized ^{13}CMRSI (HP-^{13}CMRSI), a non-equilibrium isotope distribution (positron emitting isotope, e.g. in ^{18}fluorodeoxyglucose (^{18}FDG); HP (stable) ^{13}C isotope magnetization) is introduced exogenously, with minimal invasion. Then, the (relatively slow) regional approach to isotope equilibrium is mapped using spatially encoded detection. The evaluation of generally much faster steady-state ("equilibrium") *unidirectional* fluxes must be accomplished with proper modeling (14,15,17,27,28). By far the most common example is the inference of the metabolic rate (consumption) of glucose, MR_{glc} (in μmol min^{-1} g^{-1}), from the *net* metabolic rate (uptake) of ^{18}FDG (27). In the human prostate tumor, the [1-^{13}C]pyruvate to [1-^{13}C]lactate conversion rate constant is 0.045 s^{-1} (15). With rigorous modeling, this can yield the lactate dehydrogenase flux (14). In particular, the ^{31}PMRSI modality offers the unique opportunity to measure steady-state unidirectional fluxes completely non-invasively. This takes advantage of the magnetization transfer (MT) phenomenon. An RF pulse is used to selectively perturb only certain molecular nuclear magnetization from equilibrium. Monitoring the (relatively slow) magnetization recovery with spatial encoding allows mapping of faster metabolic fluxes, again with proper modeling (17,29,30). For example in the brain, the integrated cellular creatine kinase flux and ATP production/consumption rates have been determined (17).

Spatial resolution

Extant metabolic imaging has revealed a tremendous amount about normal and pathological biochemistry, as it actually exists *in vivo*. However, new approaches can be attractive. The PET and HP-^{13}CMRSI modalities are costly. Typical nominal spatial resolutions and voxel volumes for human modalities are the following: ^{31}PMRSI, $(1.3\ cm)^3$ = 2.2 mL (17); ^{1}HMRSI, $(1\ cm)^3$ = 1 mL (20); SPECT, $(1\ cm)^3$ = 1 mL (16); HP-^{13}CMRSI, $(7\ mm)^3$ = 340 μL (15); PET, $(5\ mm)^3$ = 125 μL (16); ^{23}NaMRSI, $(4\ mm)^3$ = 64 μL (19). These are often insufficient for discriminating significant human anatomy. For example, the cerebral gray matter (GM)/white matter (WM) boundary usually cannot be clearly distinguished. In comparison, MRI – generated from the relatively strong ^1H_2O signal – commonly provides higher spatial resolution: $(1\ mm)^3$ = 1 μL or better. Metabolic images are almost always accompanied by high-resolution MRI (sometimes computed tomography) views of the same tissue. Therefore, though MRI is relatively inexpensive (compared with PET and HP-^{13}CMRSI) and employs no ionizing radiation, it is understandably often thought of as providing only anatomical and/or vascular information. Of course, it has long mapped some tissue functions, as in *ciné* cardiovascular MRI and *functional* MRI. The new metabo-CESL/CEST techniques approach anatomical ^1H_2O resolution (22), since they employ this strong signal for indirect metabolite detection.

^1H_2O mapping of NKA flux

Here we introduce a method exploiting a newly discovered aspect of the biology of water itself – active trans-membrane cycling. The (dynamic-contrast-enhanced) DCE-MRI ^1H_2O method is in wide clinical use. It employs any of a number of approved paramagnetic, monomeric Gd(III) chelates as contrast agents (CAs). For tissues manifesting extensive CA extravasation, a proper pharmacokinetic analysis of the CA bolus DCE-MRI time-course yields the mean lifetime (τ_i) of water molecules inside the cells within a voxel (31). The reciprocal (τ_i^{-1}) is the first-order rate constant (k_{io}) for the unidirectional, *equilibrium* cellular water molecule efflux. We have recently documented the evidence, from enzymatic manipulations spanning a number of different cell types and models (from cells to animals to humans), that the magnitude of k_{io} is proportional to P-type ATPase turnover (32). This is likely due to active transmembrane water cycling that accompanies the osmolyte cycling driven by the membrane ion pump (32,33).

Because the normal blood–brain barrier is CA impermeable, cerebral DCE-MRI data do not directly yield τ_i. However, the mean capillary water lifetime (τ_b) is readily determined. Fortunately, the metabolic activity of cerebral neurons is exquisitely symbiotically connected with those of neuroglia (oligodendrocytes, astrocytes) and thence capillary endothelial cells (34–37) – all within synaptic proximities. The terms "neuro*vascular* unit" and "glio*vascular* unit" have been coined (36) to connote this. Here, we present results from normal and multiple sclerosis normal-appearing (MS-NA) brain, along with MS lesion and glioma tumor, indicating that τ_b^{-1} (k_{po}) is proportional to metabolic turnover within the neurogliovascular unit. We show the first human brain k_{po} maps (40 μL voxels), and present evidence that these are metabolic flux maps at ^1H_2O resolution.

TECHNICAL BACKGROUND

Since many different principles are involved here, we present some technical background material.

Mean brain intra-capillary blood water molecule lifetime (τ_b)

The average erythrocyte speed through cerebral cortical capillaries is 2 mm s^{-1} or less (38–40): this measures blood velocity. In a common (1 mm)^3 high-resolution human ^1H_2O MRI voxel, a conservatively small estimate of the average, tortuous capillary path-length is 2 mm (40,41). Thus, the mean voxel transit time for a blood water molecule is at least 1 s. Many things happen to the molecule during this period. The mean lifetime inside an erythrocyte (τ_i) is 10 ms (42–45). By equilibrium mass action, for a 40% hematocrit the mean plasma lifetime before entering a red cell (τ_p) is 15 ms. Thus, any given water molecule enters and leaves erythrocytes about 40 times during its voxel passage (also, the entire red cell water content is exchanged ~100 times). The 3D Einstein diffusion equation, $\langle r^2 \rangle = 6Dt_D$ (46), allows estimation of H_2O molecule capillary wall encounter frequency: r is the capillary radius, D the water diffusion coefficient, and t_D the average time to diffuse a distance r. Inserting the mean feline r value, 2.6 μm (40), and a conservatively small D value (1.5 μm^2 ms^{-1}, half the pure water D), we obtain $t_D = 0.8$ ms. Even an H_2O molecule in the center of the capillary lumen would encounter the capillary wall more than 1000 times during its voxel passage. It is a very good approximation that capillary blood water is "well mixed." Thus, we can estimate the probability of a water molecule escaping the capillary. The τ_b inverse, τ_b^{-1}, is the unidirectional first-order rate constant, k_{po}, for water extravasation (47). For a well-mixed lumen, this is $\tau_b^{-1} = P_W^{\dagger}[A_{ca}/V_{ca}]$, where $P_W^{\dagger}$ is the transendothelial water permeability coefficient, A_{ca} the *individual* capillary surface area, and V_{ca} the *individual* capillary lumen volume (48). For a cylindrical microvessel: $\tau_b^{-1} = 2\ [P_W^{\dagger}/r]$. Some time ago (49), we noted that an r = 2.6 μm and a primate $P_W^{\dagger}$ value of 2 μm s^{-1} (50,51) predict 650 ms for τ_b. The k_{po} (τ_b^{-1}) value (1.5 s^{-1}) corresponds to about 78% probability (=100[1 − exp ($-k_{po}t$)]: t is the capillary transit time (~1 s)) that any given water molecule will exchange out of the blood space (to be replaced by an extravascular H_2O molecule) during its capillary passage. Because blood velocity causes no net change in the number of (indistinguishable) capillary H_2O molecules, the τ_b quantity is not influenced by the blood flow (F; CBF) magnitude. This contrasts with the situation for the extraction of labeled water (50), which is surely "perfusion limited."

It is important to note that $P_W^{\dagger}/r$ is also independent of the *intensive* capillary density ($\rho^{\dagger}$) property. With tracer studies (e.g. intracarotid $^{15}OH_2$ (50)) and sacrificial autoradiography (e.g. IV ^3HOH (52)), one obtains the intensive $P_W^{\dagger}S$ product, where S is the *total* region-of-interest (ROI) vascular surface area per unit tissue volume – dependent on the vascularity. The latter is measured by the blood volume fraction (v_b, CBV): the $\rho^{\dagger}V$ product (V is the *mean* V_{ca}). In $P_W^{\dagger}/r$, r is the *mean* ROI vascular radius, and is related only to the V factor of the $\rho^{\dagger}V$ product. Thus, theory demands that τ_b is independent of $\rho^{\dagger}$, and therefore a potentially powerful new type of imaging biomarker: we characterize it as *supra-intensive*. We show below that k_{po} is also experimentally independent of v_b, a very meaningful finding, and that it can distinguish cerebral pathology undetectable with ordinary intensive biomarkers.

Inter-compartmental ^1H_2O exchange effects in *in vivo* MR

It has been known for 40 years that a sufficiently concentrated paramagnetic solute localized in a cell suspension extracellular space can cause non-mono-exponential longitudinal and/or transverse ^1H_2O relaxation. A two-site exchange (2SX) analysis of the recovery yields τ_i, the mean intracellular water molecule lifetime (reviewed in (32,43–45)). This is equilibrium trans*cytolemmal* water exchange. Longitudinal relaxation for yeast cell samples (33,49,53) exemplifies this. The extracellular CA increases the intrinsic outside water proton signal ($^1H_2O_o$) longitudinal relaxation rate constant, R_{1o} ($\equiv (T_{1o})^{-1}$). Though we generalized and systematized the exchange picture (and introduced the term) only in 1999 (54), this approach increases the longitudinal transcytolemmal "shutter-speed," τ_{1c}^{-1} ($\equiv |R_{1o} - R_{1i}|$), sufficiently that this water exchange NMR system is moved out of its fast-exchange-limit (FXL) condition ($\tau_{1c}^{-1} \ll (\tau_i^{-1} + \tau_o^{-1})$); R_{1i} is the intrinsic inside ($^1H_2O_i$) relaxation rate constant). A sufficient outside CA concentration, [CA_o], allows the NMR system to reach the slow-exchange-regime (SXR) condition. This is characterized by non-mono-exponential magnetization recovery, but is distinct from the slow-exchange- and no-exchange-limit conditions (31,33,43,47,55). It is quite customary to achieve the SXR condition with cell suspensions (33,43–45,49), but there is no convincing evidence that the SXR can be reached *in vivo* with approved CAs. However, it has been shown that when the [CA_o] value is only modest, and the system can attain only the fast-exchange-regime (FXR) condition, it is still possible to measure τ_i by *varying* τ_{1c}^{-1} (by varying [CA_o]) (49). The FXR condition features mono-exponential longitudinal recovery: i.e., R_1 is single valued, but with a non-linear [CA_o] dependence. In the FXL condition, this dependence is linear (31,33,43,49,54). The *in vivo* implementation of these principles generally employs some variant of DCE-MRI, the serial acquisition of T_1-weighted images before, during, and after a bolus CA injection. The common tracer paradigm (TP) pharmacokinetic analysis of an ROI or voxel signal intensity time-course imposes the assumption that all exchange systems remain in their FXL conditions. This denies access to τ_b, or τ_i (each is held effectively zero in the FXL), and causes systematic changes in other pharmacokinetic parameters, such as v_b. However, shutter-speed paradigm (SSP) pharmacokinetic analysis allows that τ_b and τ_i are finite, and relieves the systematic distortions of other biomarkers. Overviews of these concepts have been published (31,33,43,55).

It was gratifying when, in 1997, multiple infusions of an intravascular CA were used to vary the murine brain trans*endothelial* shutter-speed, τ_{1e}^{-1} ($\equiv |R_{1b} - R_{1exv}|$) ($^1H_2O_b$ and $^1H_2O_{exv}$ are the intra- and extravascular signals, respectively) and reach the FXR condition ($\tau_{1e}^{-1} \rightarrow (\tau_b^{-1} + \tau_{exv}^{-1})$; τ_{exv} is the mean extravascular water molecule lifetime) for this water exchange system. Variation of the plasma CA concentration, [CA$_p$], allowed the exchange kinetics to be measured (56). The cortical τ_b value we calculate from these results is 295 ms – of the magnitude we had earlier predicted from literature parameters (see above). In 2002, an approach using a single intravascular CA injection was demonstrated in the rat (57). The [CA$_p$] value was not varied, but the acquisition was combined with an arterial spin labeling (ASL) variant. This approach yields only $P_W^{\dagger}S$ and, because ASL is used, the F value must be included in order to obtain $P_W^{\dagger}S$ correctly (57). In 2003, we introduced an SSP DCE-MRI method whereby a single CA bolus injection can be used to determine human brain τ_b (58). This approach is used here. Seven years ago, the water exchange index (WEI), an approximate, dimensionless, non-linear τ_b^{-1} estimate, was demonstrated in the mouse, an approach also requiring a single intravascular CA injection (59). Recently however, the authors of Reference 59 themselves showed that, unfortunately, the WEI approximation formally depends on the v_b value (60). As noted above, an important feature of the actual τ_b^{-1} (k_{po}) biomarker is its v_b independence if r does not vary.

Indirect detection

There are crucial differences between the tracer and shutter-speed paradigms. Classic tracers (radiolabeled molecules, electron-dense compounds, etc.) are detected directly: the tracer molecule is also the signal molecule. Though the CA of DCE-MRI plays the tracer pharmacokinetic role, it is detected indirectly – via its effect on the ^1H_2O signal. Thus, the CA is the tracer molecule but water is the signal molecule. These species are never distributed equally in tissue: water is in every compartment, each of which contributes to the ^1H_2O signal. For the classic solute TP, water is not molecular: it is a *continuum* filling tissue spaces. Furthermore, the compartmentalization of the classic tracer is not intrinsic to its signal: one cannot tell if the molecule is intra- or extravascular. However, CA compartmentalization is inherently encoded in the DCE-MRI time-course. Three simultaneous signals ($^1H_2O_b$, $^1H_2O_o$, and $^1H_2O_i$) and their sequentially varying T_1 values report the time-varying [CA] values in each compartment CA enters (31,55). Thus, the imposition of a tracer analysis on DCE-MRI data joins contradictory postulates: unknown versus known CA compartmentalization. The only reconciliation is by the assumption that all water exchange systems are in FXL conditions. If τ_b is assumed to be effectively zero, the vascular CA compartmentalization is "short-circuited," as if CA is both intra- and extravascular – a tracer-like ambiguity. These principles also apply to metabo-CESL/CEST (61).

Chemical equilibrium measurement

Another important difference is experimental. For classic water tracers (e.g. $^{15}OH_2$ (50)), the study is initiated with a non-equilibrium isotope compartmental distribution, and the kinetics of the tissue's approach to equilibrium are monitored by detecting only the labeled water. In DCE-MRI, there is no compartmental selection in the initial water proton magnetization perturbation: all ^1H_2O signals are (usually) inverted, and the return to magnetic equilibrium of each of them is monitored simultaneously. Only magnetization equilibrium is perturbed. These methods can lead to common parameters (e.g. $P_W^{\dagger}$ here), and thus can support each other. However, the experimental results must be analyzed with different paradigms as appropriate. For example, though the SSP assumes that brain capillary water is "well mixed" – justified above – it does not require the same assumption of extravascular water, which is in fact not well mixed. Although τ_i and τ_o values are typically hundreds of milliseconds, that of τ_{exv} is typically tens of seconds (see later) – because of the relatively sparse microvessel density. Yet the extravascular ("parenchymal") MR system is in the fast-exchange-limit condition even though transcytolemmal water exchange is not particularly fast. With no extravascular CA, the τ_{1c}^{-1} values are much smaller than ($\tau_i^{-1} + \tau_o^{-1}$). Thus, the non-well-mixed nature of the parenchyma is of no consequence to the DCE-MRI experiment, but "unstirred layer" effects can be significant for $^{15}OH_2$ re-intravasation kinetics, or for any tracer study (12).

Active trans-membrane water cycling

There is obviously considerable interest in the brain capillary τ_b (k_{po}^{-1}) quantity. From the above, we see that τ_b variation can reflect a change in capillary r, in $P_W^{\dagger}$, or in both. Vasodilation or vasoconstriction (r alteration) would respectively decrease or increase k_{po} (τ_b^{-1}). However, the rate constant for r changes is orders of magnitude smaller than k_{po} itself (33,62). Changes in k_{po} not attributable to capillary size alteration are ascribed to $P_W^{\dagger}$ variation and, until recently, this has been conceived as resulting from alterations in passive molecular processes ($P_W^{\dagger}$(passive)). These include (a) paracellular water passage through endothelial tight junctions, (b) simple, transcellular water diffusion across cell membrane lipid bilayers, and (c) transcellular transport through membrane aquaporin protein water channels (63,64) and/or transcellular leakage through membrane transporters (65). However, NMR studies have recently revealed the *cell membrane* water permeability coefficient (P_W) to have an active component (P_W(active)) that dominates over the passive component (32,33). This is due to active transmembrane water cycling accompanying active transmembrane osmolyte cycling, which is paced by the driving cell membrane P-type ATPase ion pump (32,33). For animal cells, this is NKA (32,33,66–68). The molecular mechanism likely involves water cotransporting membrane symporters (69,70), and supports a cycling flux of 10^{12} water molecules s^{-1} per cell.

EXPERIMENTAL

Subjects

Healthy (2M/4F, 30 (±10) years), relapsing–remitting-MS (RRMS) (2M/4F, 46 (±7) years, 18–55 years), and glioblastoma multiforme (GBM) (3M/2F, 19–57 years) subjects gave informed consent to OHSU Institutional Review Board approved protocols. The MS group was early in disease, but with positive MRI findings. An additional 52 year old female late-stage RRMS subject was also studied. The GBM subjects had prior surgical biopsies or resections and chemo-radiation therapy.

Healthy and MS subject DCE-MRI

A 7 T whole-body MRI instrument (Siemens, Erlangen, Germany), with quadrature transmission and 24-channel phased-array receive head RF coils, was used. Dynamic measurements employed a single-slice inversion recovery (IR) turboFLASH technique (71), sampling magnetization at eight post-inversion times (*TI* values): the inversion pulse was non-selective. The 128 × 96 image matrix covered a (256 × 192) mm^2 field of view (FOV) (nominal pixel, (2 mm)^2), and a 6° flip angle RF pulse selected a 10 mm transverse slice superior to the lateral ventricles (nominal voxels, (2 × 2 × 10) mm^3 = 40 μL). Gadoteridol (ProHance; Bracco Diagnostics, Cranberry, NJ) was injected into an antecubital vein catheter at 1.0 mL s^{-1} using a power injector (Medrad, Warrenville, PA) to deliver a dose of 28 μmol kg^{-1} (typically ~5 mL), followed by a 20 mL saline flush at the same rate. For each CA injection, 50 IR image sets were collected with 2.3 s temporal resolution. Total acquisition time was 1.9 min. Parametric R_1 maps were calculated on a voxel basis by fitting the signal magnitude at each *TI* with a full Bloch simulation incorporating all RF pulses and delays. The IR was modeled with a two-parameter single exponential, using a gradient expansion algorithm.

GBM subject DCE-MRI

Data were acquired using a 3 T Tim Trio (Siemens) instrument, body transmit and 12-channel phased-array head receive RF coils, and a full volume 2D gradient-recalled-echo echo-planar imaging sequence. Non-selective IR pulses were sampled at 24–36 *TI* values. The 128^2 image matrix covered a 256^2 FOV (nominal (2 mm)^3 isotropic resolution; 8 μL nominal voxels) (72). ProHance DCE-MRI was similar to the controls and MS subjects. The next day, the intravascular FeO nanoparticle CA ferumoxytol (Fe-tol; Feraheme; AMAG Pharmaceuticals, Waltham, MA) was used. Points were obtained in the CA steady states before and after three IV Fe-tol injections (73), fractionated into doses (1:2:4) totaling 4 mg(Fe) kg^{-1} (72 μmol(Fe) kg^{-1}, ~12 nmol(Fe-tol) kg^{-1}), each at 3 mL s^{-1}. The 5 min acquisitions were initiated 120 s after each Fe-tol injection, during the steady-state period when [CA$_p$] was uniform and constant. (The 14 hour Fe-tol plasma $t_{1/2}$ ensures [CA$_p$] is larger after each successive injection.) All four acquisitions were completed in 40 min. Pre- and post-CA session R_1 maps were co-registered to pre-CA T_1-w MPRAGE maps using rigid body transformations. This protocol yielded four pharmacokinetic time points, sufficient to characterize high quality R_{1t} versus R_{1b} measurements such as those in NA brain (see Fig. 5 later). This sparse temporal sampling approach was originally designed for optimization of brain coverage and spatial resolution. Unlike gadoteridol (GdHPDO3A) DCE-MRI, in which [CA$_p$] reaches large values only transiently – during the first pass (Fig. 1), Fe-tol steady-state [CA$_p$] can attain quite high and sustained levels.

DCE-MRI pharmacokinetic modeling

Non-linear modeling (IDL; Exelis, Boulder, CO) was used to extract accurate estimates of $R_{1\mathrm{exv}}$, v_b, and τ_b for selected ROIs (and also on a voxel-wise basis) using the equation

$$\begin{aligned} R_{1t}(t) = {} & ½\left[\left\{R_{1\mathrm{exv}} + R_{1b}(t) + \tau_b^{-1} + p_b/[\tau_b(1-p_b)]\right\}\right. \\ & - \left(\left\{R_{1\mathrm{exv}} - R_{1b}(t) - \tau_b^{-1} + p_b/[\tau_b(1-p_b)]\right\}^2\right. \\ & \left.\left. + 4p_b/\tau_b^{2}(1-p_b)\right)^{1/2}\right]. \end{aligned} \qquad [1]$$

p_b is the mole fraction of tissue water in blood (v_b = $p_b f_W$, where f_W is the tissue volume fraction accessible to mobile aqueous solutes (55)). The independent modeling measure is

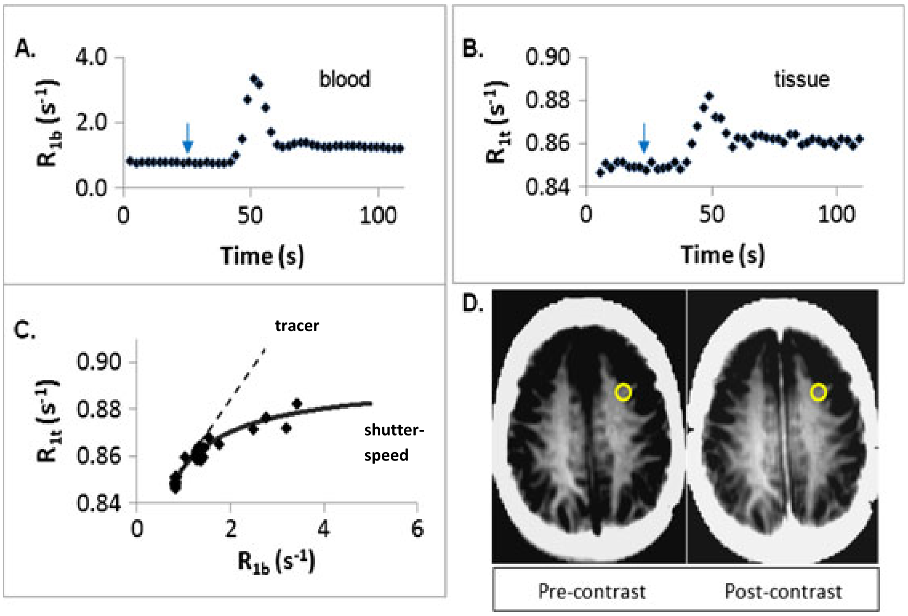

Figure 1. Normal ^1H_2O DCE-MRI data. These arise from a 22 year old female control subject. Panel D shows axial R_1 maps pre- and at one point post-CA administration. The CA injection is indicated by blue arrows in the R_1 time-courses in panels A and B (A, blood ROI R_{1b} response function; B, WM ROI R_{1t} response function). The WM ROI is indicated by the yellow circles in panel D. Panel C plots the R_{1b} dependence of R_{1t} from A and B. The points exhibit a clear deviation from the linearity demanded by the TP, which embodies the FXL constraint (dashed line). The points are well fitted with the SSP (solid curve), Equation [1], with parameters given in the text. Population-averaged parameter values are presented in Table 1.

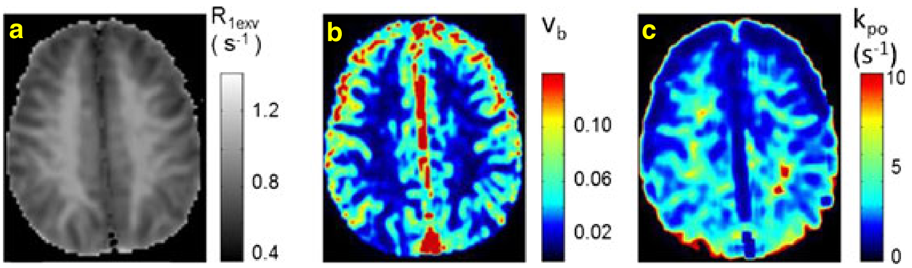

Figure 2. Normal parametric maps. SSP maps for the healthy control subject of Figure 1. (a) R_{1exv} (intrinsic, extravascular R_1), (b) v_b (blood volume fraction), and (c) k_{po} (τ_b^{-1}) (τ_b is the mean capillary water molecule lifetime). The k_{po} rate constant map displays ongoing resting-state metabolic activity.

$R_{1b}(t)$, which is determined by $[CA_b](t)$ (defined by $R_{1b}(t) = R_{1b0} + r_{1b}[CA_b](t)$, with R_{1b0} the pre-CA R_{1b} and r_{1b} the CA relaxivity). $R_{1b}(t)$ was measured directly from an R_1 map ROI placed fully within the sagittal sinus. Equation [1] describes a 2SX NMR system spanning the FXL and FXR conditions, depending on $[CA_b]$. For elaboration, see References 31 and 42.

RESULTS

k_{po} and v_b values in normal and normal-appearing MS brain

Figure 1 displays 7 T ^1H_2O IR turboFLASH DCE-MRI data, and SSP analysis (58), for a 22 year old female control subject. Panels A and B show R_1 time-courses: GdHPDO3A was injected at about 35 s (arrows). The Figure 1(A) data are from a blood (sagittal sinus) ROI, those in Figure 1(B) from the normal white matter (NWM) ROI indicated by circles in panel D; axial R_1 maps before and after CA administration. The CA passes through the brain without appreciable extravasation. Panel C shows the R_{1b} dependence of R_{1t} from Figure 1(A), (B). If the TP obtained, the R_{1t} vs. R_{1b} plot would be linear. This is indicated by the dashed line in Figure 1(C). The non-linear data are well fitted with the 2SX SSP expression of Equation [1] ($f_W = 0.8$), spanning the FXL and FXR conditions (31,42,55,58) (solid curve)] with τ_b = 560 ms, v_b = 0.018, and R_{1exv} = 0.85 s^{-1} (the intrinsic extravascular ^1H_2O R_1). If the TP is forced to the data, the dashed FXL line must pivot about their origin ($R_{1b}(0)$, $R_{1t}(0)$) and its slope, v_b, is significantly decreased. In this case, the TP gives $v_b = 0.015$, a 17% underestimation. Of course, TP also denies access to τ_b, since it assumes it zero.

Figure 2 displays axial voxel-by-voxel parametric maps for the subject of Figure 1. The biomarkers are (a) R_{1exv}, (b) v_b, and (c) k_{po} (τ_b^{-1}). As expected, R_{1exv} is greater in NWM than in normal gray matter (NGM), and the v_b map exhibits greater NGM (0.03) than NWM (0.01) values. The latter approximate rather well absolute CBV fractions, not relative values. Though such maps are quite important, they exhibit the natures of the R_{1exv} and v_b properties. The larger NWM R_{1exv} values reflect the greater macromolecular volume fractions of NWM (74) and the larger NGM v_b values reflect the well-known greater NGM vascularity. As far as we are aware, Figure 2(c) is the first k_{po} map. As discussed above, τ_b is a supra-intensive parameter. It is very interesting that the k_{po} map (Fig. 2(c)) exhibits greater intensity in NWM, averaging 3.0 s^{-1}, than in NGM, 2.5 s^{-1}.

Figure 3 shows the voxel-by-voxel k_{po} versus v_b scatter plot of many of the data of Figure 2(b), (c). The voxels were chosen from 50^2 in a square slab ROI centered on and covering about 75% of the brain image slice of Figures 1 and 2. The R_{1exv} relaxation rate constant spectrum (histogram) was used to assign the voxels (74). The 649 voxels with R_{1exv} values between 0.80 and 0.92 s^{-1} were identified as NWM, and yield the pink points in Figure 3. The 670 voxels between 0.62 and 0.72 s^{-1} are labeled NGM, and give the olive points in Figure 3. As expected, the NWM points cluster below v_b = 0.02. The NGM points cluster about a v_b value (0.06) somewhat greater than expected, because a number represent voxels with some partial-volume averaging of vessels larger than capillaries – especially near the cortical surface (Fig. 2(c)). Interestingly, the NGM k_{po} (τ_b^{-1}) values are essentially independent of v_b, and the NWM v_b values are essentially independent of k_{po}. The basically horizontal and vertical orthogonal NGM and NWM clusters are consistent with parameters not numerically correlated by data fittings. The interesting trends seen in Figure 3 are physiological. The parameter $v_b = \rho^{\dagger}V$. By definition, k_{po} is $\rho^{\dagger}$ independent, and is dependent on only $V^{-1/2}$. Since k_{po} is experimentally independent of v_b, k_{po} variations must be due to $P_W^{\dagger}$ variations (Background). In NWM voxels these are large but v_b is small and apparently regulated (likely $\rho^{\dagger}$ regulation), while in NGM voxels k_{po} seems regulated. The very slight downward slope of the green point cluster at larger v_b is due to the partial-volume averaging mentioned above. Larger v_b values reflect larger mean *r* values, and there is a slight k_{po} decrease due to this, but mostly k_{po} is constant in NGM.

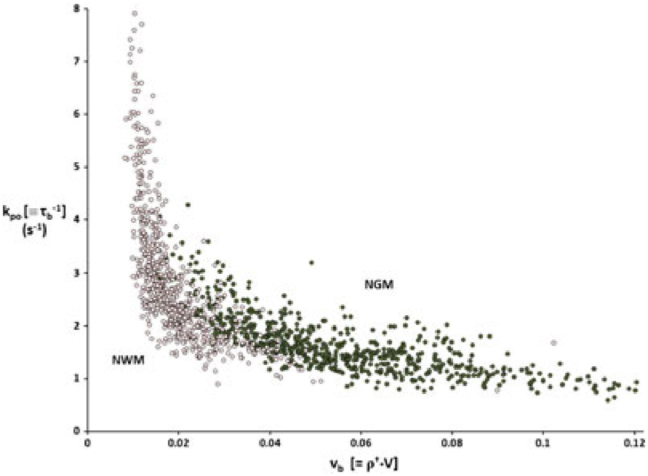

Figure 3. Normal scatter plot. The plot of k_{po} (τ_b^{-1}) values versus v_b values for the pure NWM (pink) and NGM (olive) voxels from Figure 2 (b), (c). v_b is the capillary density–volume product, $\rho^{\dagger}V$. The NWM and NGM assignments were made from the R_{1exv} (Fig. 2(a)) value histogram (not shown; see text). Parametric interdependence would be manifest as sloped clusters. The basically orthogonal NWM and NGM clusters signify the k_{po} and v_b biomarkers are essentially independent of each other, and this means k_{po} is dominated by capillary wall water permeability (see text).

Now, we turn to population averages. Table 1 presents (about 3.6 mL) ROI biomarker values averaged for six healthy controls and six RRMS subjects with "non-enhancing" WM lesions. Precision is generally quite good: the SEMs listed are due mostly to inter-subject variation. The fact that the k_{po} values in NWM and NGM are more similar than the v_b values is due to the aforementioned supra-intensive nature of τ_b. The R_{1exv} values are reduced in NGM, normal-appearing gray matter (NAGM), and MS lesions because of decreased macromolecular volume fractions (74). The v_b values are increased in normal-appearing white matter (NAWM) and NAGM, and decreased in MS lesions. More interesting is the fact that k_{po} is decreased in MS-NAWM and MS-NAGM, and even more-so in lesions.

For a cylindrical capillary, $k_{po} = 2P_W{}^\dagger r^{-1}$: the quantity r is a 1D measure of capillary size. With a conservatively large r value (3 μm (39,40)), $k_{po} = 0.7P_W{}^\dagger$ (k_{po} in s^{-1}, $P_W{}^\dagger$ in μm s^{-1}). With a typical $P_W{}^\dagger$ value (2 μm s^{-1} (50,51)), $k_{po} = 4r^{-1}$ (r in μm). Thus, k_{po} is linearly related to both $P_W{}^\dagger$ and r^{-1}, with different coefficients. In the Discussion section, we compare concomitant relative (%) changes in the population-averaged v_b and k_{po} parameters for the NGM → NAGM (Table 1) transition. A deductive quantitative analysis shows that the k_{po} decrease is dominated by a $P_W{}^\dagger$ decrease. The analogous exercise indicates an even greater $P_W{}^\dagger$ decrease in MS-NAWM. k_{po} ($\tau_b{}^{-1}$) is dominated by the $P_W{}^\dagger$ factor, not the r^{-1} factor.

Decreased k_{po} in the MS lesion

In non-enhancing MS lesions, the k_{po} value is decreased even further: the average for the six Table 1 RRMS subjects is 1.8 s^{-1}. However, these represent relatively early-stage disease. Figure 4 shows results for a 52 year old female late-stage RRMS subject. Quite large chronic demyelinated WM lesions appear hypointense in the R_{1exv} map (Fig. 4(a)) – indicating extensive macromolecular loss, consistent with demyelination and gliosis. These lesions are many months past their last high CA-enhancement stage. The v_b map (Fig. 4(b)) is rather similar to that of the control (Fig. 2(b)), but reduced (<0.01) in lesion areas and NAWM. However, the k_{po} map (Fig. 4(c)) is dramatically altered. Unlike NWM (Fig. 2(c)), the WM region is extremely hypointense. The k_{po} values in the lesions themselves (~1.5 s^{-1}) are *decreased* below the MS-NAWM mean (2.2 s^{-1}) and even the RRMS lesion mean (1.8 s^{-1}) (Table 1). Furthermore, compared with the RRMS NAGM mean (2.0 s^{-1}) (Table 1), the k_{po} values (~2.9 s^{-1}) are considerably *increased* in this advanced subject NAGM. (It is hard to discern the NAWM situation because the lesions are so large.)

Decreased k_{po} in the GBM tumor

For GBM capillaries, clinical monomeric Gd(III) chelate CAs extravasate too rapidly to allow k_{po} determination. Thus, we used the intravascular, coated superparamagnetic iron oxide nanoparticle Fe-tol as CA (73). This agent has a molecular mass of 750 000 Da (10^3 times that of GdHPDO3A; 588 Da). Its K^{trans} in normal and NA brain tissue is ~10^{-8} min^{-1} (75). (The biomarker $K^{trans} \approx P^\dagger_{CA}S$, where $P^\dagger_{CA}$ is the endothelial CA permeability coefficient (76).) During the first pass, it remains intravascular even in very advanced GBM tumors with extremely permeable capillaries. Figure 5 shows results from a 52 year old male GBM subject. In the center is an R_1 map obtained 30 min after GdHPDO3A injection. The large CA-enhancing tumor is clearly visible at the bottom left. Twenty-four hours after GdHPDO3A, the subject received IV Fe-tol. Inset are data (points) obtained from four representative ROIs (frontal WM, thalamus, putamen (white ellipses), and tumor (red circle)) during the Fe-tol injections. Each plot shows the R_{1b} dependence of R_{1t} (as in Fig. 1(C)). If the TP ($\tau_b \rightarrow 0$) held, the R_{1t} vs. R_{1b} plots would be linear. None are, and all are well fitted by Equation [1] 2SX SSP expression curves with R_{1exv}, v_b, and τ_b varied. The R_{1exv}, v_b, and τ_b parameter values returned are 1.24 s^{-1}, 0.008, 0.29 s (frontal WM); 0.99 s^{-1}, 0.013, 0.32 s (thalamus); 0.94 s^{-1}, 0.014, 0.43 s (putamen), and 0.77 s^{-1}, 0.028, 1.52 s (tumor). For five subjects, the population- and ROI-averaged parameter values are given in Table 1. For this 3 T study the R_{1exv} values are greater than the normal and MS brain 7 T entries. Tissue macromolecular relaxivity is greater at smaller field (74). In the GBM normal appearing (GBM-NA) brain, the v_b values are generally smaller than normal. They are large in the tumor.

Table 1. Population-averaged resting-state human brain ROI parameter values

	SSP DCE-MRI (^1H_2O)			
	R_{1exv} (s^{-1})	v_b	τ_b (s)	k_{po} (τ_b^{-1}) (s^{-1})^c
Healthy controls (n = 6)[a]				
NWM	0.831 (±0.021)	0.014 (±0.002)	0.35 (±0.04)	3.2 (±0.56)
NGM	0.679 (±0.015)	0.031 (±0.004)	0.41 (±0.06)	2.9 (±0.59)
Relapsing–remitting MS (n = 6)[a]				
NAWM	0.810 (±0.022)	0.019 (±0.002)	0.48 (±0.05)	2.2 (±0.20)
NAGM	0.672 (±0.009)	0.045 (±0.004)	0.50 (±0.03)	2.0 (±0.13)
Lesion	0.624 (±0.009)	0.012 (±0.003)	0.59 (±0.14)	1.8 (±0.45)
Glioblastoma (n = 5)[b]				
NA-frontal WM	1.10 (±0.027)	0.008 (±0.001)	0.44 (±0.04)	2.6 (±0.31)
NA-thalamus	0.90 (±0.009)	0.017 (±0.001)	0.38 (±0.05)	2.9 (±0.37)
NA-putamen	0.78 (±0.013)	0.012 (±0.005)	0.43 (±0.03)	2.5 (±0.22)
Tumor	0.67 (±0.013)	0.046 (±0.013)	≥5.6	≤0.18

[a] ProHance, 7 T.

[b] Ferumoxytol, 3 T.

[c] $\langle k_{po} \rangle$ ($\neq \langle \tau_b \rangle^{-1}$). Uncertainties are ±SEM.

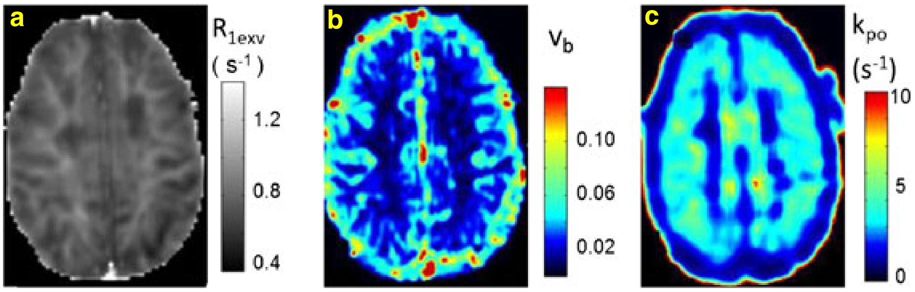

Figure 4. Late-stage MS parametric maps. SSP maps for a 52 year old female advanced RRMS subject. (a) ^1H_2O R_{1exv}: extensive, chronic WM lesions are hypointense. (b) v_b shows substantial reductions (<0.01) in the lesion areas. (c) k_{po} (τ_b^{-1}) shows striking contrast between lesions and NAGM. The k_{po} values are strongly depressed in lesion areas, and considerably elevated in cortical regions, compared with the control (Fig. 2(c)). The k_{po} map suggests low resting-state metabolic activity in these significantly demyelinated lesions.

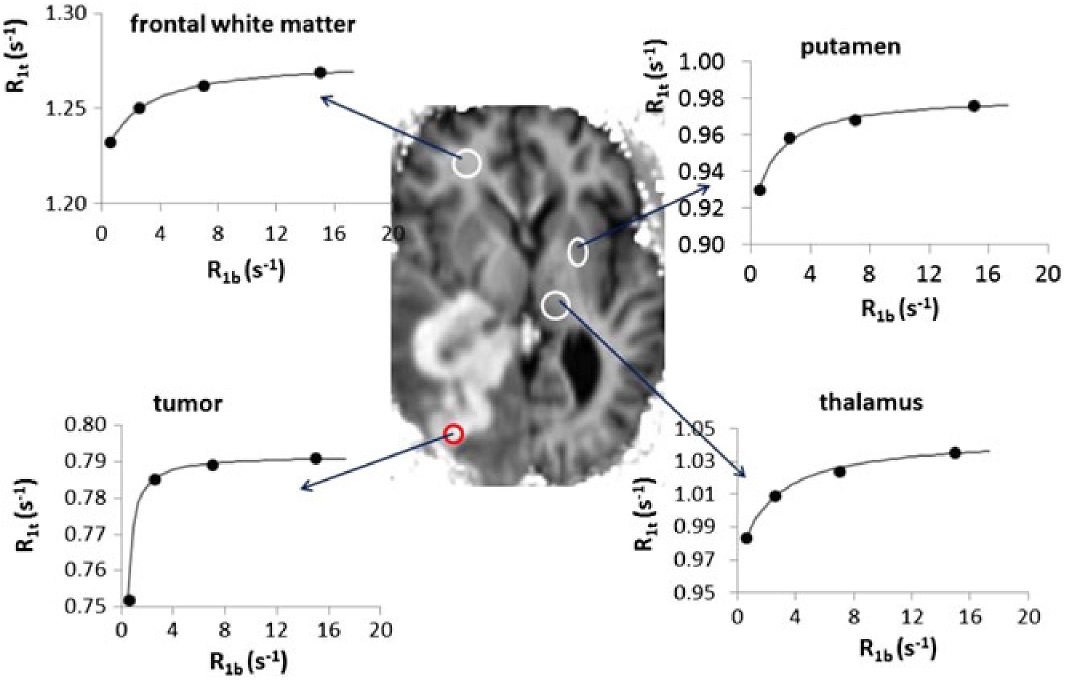

Figure 5. GBM ^1H_2O DCE-MRI data. These arise from a 52 year old male glioblastoma subject. The axial R_1 map in the center was obtained 30 min after injection of a monomeric Gd(III) chelate CA. The enhancing tumor is clearly visible in the image bottom left. The insets show R_{1t} versus R_{1b} plots (as in Fig. 1(C)) before and after injections of an intravascular CA, administered well after the Gd(III) CA had cleared. The ROIs giving rise to the plots are indicated by circles and an oval. The plots from frontal WM, putamen, and thalamus ROIs have hyperbolic shapes similar to that in Fig. 1(C). The points exhibit clear deviations from the linearity demanded by the TP. However, the tumor plot exhibits even sharper hyperbolic behavior. The points are well fitted with the SSP (Equation [1]; solid curves): parameter values are given in the text. Population-averaged parameter values are presented in Table 1.

The k_{po} values in the GBM-NA brain are fairly normal. This supports the general accuracy of the three Fe-tol injection steady-state protocol. (The latter favored spatial resolution over pharmacokinetic temporal resolution, just the opposite of the GdHPDO3A protocol used to obtain the Table 1 normal and MS-NA values.) Importantly, the Figure 5 tumor tissue k_{po} is decreased by more than a factor of five. The example tumor ROI shows why: the R_{1t} vs. R_{1b} plot has a much sharper hyperbolic shape. Though the Fe-tol protocol yielded only four pharmacokinetic points, this behavior is confirmed by the population ($n = 5$) averaging (Table 1), where the tumor k_{po} decrease is over an order of magnitude. Since there is likely a family of fittings of the four data points for which the k_{po} values are even smaller, it is best to consider the Table 1 GBM tumor k_{po} entry as an upper limit. The very large GBM tumor tissue τ_b values were unexpected. Future Fe-tol protocols will acquire more than four points while still achieving full brain coverage and good spatial resolution.

The fact that k_{po} decreases in MS lesions and in GBM tumors is very significant. We show below that this is due to $P_W{}^{\dagger}$ decreases. However, these are both pathological tissues well known to have leaky capillaries: K^{trans} is clearly increased in each. Furthermore, the increase of the $P_{CA}{}^{\dagger}$ factor dominates K^{trans}. This is what is meant by the colloquial phrase “increased capillary permeability.” The facts that $P_W{}^{\dagger}$ decreases while $P_{CA}{}^{\dagger}$ increases mean that water and CA molecules do not exchange across the capillary wall by the same dominant mechanism. This important finding is elaborated in the Discussion section.

τ_{exv} values

Finally, equilibrium mass action demands $\tau_{exv} = \tau_b[(1 - p_b)/p_b]$, where p_b is the mole fraction of water that is vascular ($= v_b/f_W$). Combining the Table 1 v_b and τ_b values, we obtain τ_{exv} values of 19 s and 10 s for NWM and NGM, respectively. These are comparable to the first-order lifetime, 45 s, calculated (49) from the observed 31 s $t_{1/2}$ for brain parenchyma $^{15}OH_2$ intravasation (50). As detailed above, this 2SX expression does not require the assumption that parenchymal water is "well mixed," only that its MR systems are in their FXL conditions.

DISCUSSION

k_{po} variations are due to $P_W{}^{\dagger}$ differences

As noted above, the essential independence of the experimental k_{po} and v_b parameters in the Figure 3 voxel scatter plot signifies that k_{po} is dominated by capillary wall water permeability. Further, quantitative deductive analyses of concomitant population-averaged $\tau_b{}^{-1}$ ratios and v_b ratios in normal brain, MS-NA brain, GBM-NA brain, MS lesions, and GBM tumors show that variations in the capillary equilibrium water efflux rate constant (k_{po}) are dominated by differences in microvessel wall water permeability ($P_W{}^{\dagger}$), not capillary radius. Example analyses are detailed in Appendix A.

Briefly, we use the relationships $k_{po}(A)/k_{po}(B) = [P_W{}^{\dagger}(A)/P_W{}^{\dagger}(B)](r_B/r_A)$, and $[v_b(B)/v_b(A)]^{1/2} = (\rho_B{}^{\dagger}/\rho_A{}^{\dagger})^{1/2}(r_B/r_A)$, for ROIs A and B. For example, for A = NAGM and B = NGM we plot in 3D capillary property space the trace of all points that simultaneously satisfy the experimental population-averaged $k_{po}(A)/k_{po}(B)$ and $[v_b(B)/v_b(A)]^{1/2}$ ratios (Fig. A1). The experimental data are incompatible with the mean capillary radius and density simultaneously remaining invariant from NGM to NAGM. The brain literature generally indicates it more likely that chronic v_b differences are due to capillary density ($\rho^{\dagger}$) differences than to capillary dilation or constriction (r changes) (38–41). (Even in an acute hypercapnic perturbation, the microvascular radii for the dominant capillary volume fraction remain unchanged (41). The very smallest capillaries, normally effectively occluded, are opened during the hypercapnia – there is some "recruitment" – but in most capillaries there is a blood velocity increase (41).) Therefore, the Figure 1A results clearly indicate that the mean capillary water permeability in MS NAGM is reduced from its value in NGM (the NGM → NAGM transition). For equal mean capillary radii, $P_W{}^{\dagger}(\text{NAGM}) = 0.8P_W{}^{\dagger}(\text{NGM})$, $P_W{}^{\dagger}$ is reduced by 20%. Recall that r is the average for a large number of capillaries. Only 100 capillaries μL^{-1} means 4000 per 40 μL voxel. The Table 1 ROIs represent 80–100 voxels. 100 voxel ROIs in six subjects yield averages over 2 400 000 capillaries.

Capillary water exchange is dominated by transcellular pathways

There are many possible pathways water molecules can use for capillary egress and ingress. Figure 6 summarizes these. It depicts (a) paracellular water passage through endothelial tight junctions (endothelial cells are colored gray), (b) simple, transcellular water diffusion across cell membrane lipid bilayers, and (c) transcellular transport through membrane aquaporin protein water channels (63,64,77) and/or leakage through membrane transporters (65). (Inspirations for this diagram are found in References 35, 36, and 63. It emphasizes water equilibria, and is otherwise greatly simplified.) The Figure 6(d) transcellular process will be elaborated below.

The facts that, in MS lesions and GBM tumors, $P_W{}^{\dagger}$ decreases while $P_{CA}{}^{\dagger}$ increases mean that water and CA molecules exchange via different pathways. CA molecules are universally thought to employ the para(endothelial)cellular pathway (Fig. 6(a)), and we previously thought that this would be a major mechanism for water as well. In Appendix B, however, we compare k_{po} with k_{pe} (for CA extravasation) to show that, for the normal brain, by far the vast majority (>95%) of capillary water efflux (and influx) occurs via one or more transcellular processes (Fig. 6(b)–(d)). This is a fundamental finding, and we are not aware that it has been previously known.

Equilibrium transendothelial water exchange is a metabolically active process

Which, if any, of the transcellular pathways (Fig. 6(b)–(d)) dominates k_{po}? Mechanisms 6(b) and 6(c) (bilayer diffusion, and passage through trans-membrane aquaporin and/or protein channels, respectively) are passive, i.e. require no energy expenditure. However, comparison of our results with literature metabolic imaging studies of the same tissues indicates that the process measured by k_{po} is metabolically active.

This is shown in Table 2. The second and third columns repeat the Table 1 v_b and k_{po} entries and place them adjacent to results of pertinent quantitative ^{31}PMRSI (78) and ^{23}NaMRSI (19,79) studies. Because of ^{31}PMRSI spatial resolution limitations, it is important that WM/GM image segmentation be accomplished with co-registered ^1H_2O maps, and then applied to apportion the MRSI measurements (78). Such results are listed in Table 2. It is clear that k_{po} exhibits a positive correlation with tissue ATP concentration, $[ATP_t]$, comparing NWM with NGM, NWM with NAWM, NGM with NAGM, or NAWM with NAGM. For example, $[ATP_t]$ decreases from normal brain in both NAWM (13%) and NAGM (20%). The phosphocreatine concentration, $[PCr_t]$, also decreases (not shown) in rough proportion to $[ATP_t]$ (78), consistent with the maintenance of overall ATP/PCr equilibrium. In contrast, k_{po} correlates negatively with TSC, $[Na_t]$, which increases in NAWM (39%), NAGM (17%) (19), and GBM tumor (51%) (79). Since there is insignificant extracellular ATP, $[ATP_t]$ reflects $[ATP_i]$. An $[Na_t]$, TSC, increase could reflect an $[Na_i]$ increase. An $[ATP_i]$ decrease and a possible $[Na_i]$ increase signify compromised metabolism: decreased ATP hydrolysis chemical potential and trans-mural Na^+ gradient electrochemical potential, respectively. The brain k_{po} values are correlated with metabolic thermodynamic properties.

However, k_{po} is a kinetic parameter (of dimension reciprocal time). In order to validate a flux measurement, one must compare it with the gold standard flux measurement. Normal homeostatic neuronal cell metabolic rates have been measured with ^{31}PMRSI-MT, using ^1H_2O segmentation (17). For NGM, the ATP synthesis (mostly by oxidative phosphorylation, CMR_{oxphos}; Fig. 6) flux is 0.16 nmol s^{-1} μL^{-1} (17), and of course the consumption rate is the same. The fluxes between ATP and phosphocreatine (PCr) are seven times larger, 1.15 nmol s^{-1} μL^{-1} in each direction (17): integrated over the neuron, ATP and PCr are in effective equilibrium. The NGM and NWM CMR_{oxphos} values, 160 and 50 pmol(ATP) s^{-1} μL^{-1}, respectively (17), are entered in Table 2, as is the $CMR_{oxphos}(\text{NGM})/CMR_{oxphos}(\text{NWM})$ ratio, 3.2. By definition, k_{po} is proportional to the H_2O flux per capillary and v_b to the number of capillaries per unit tissue

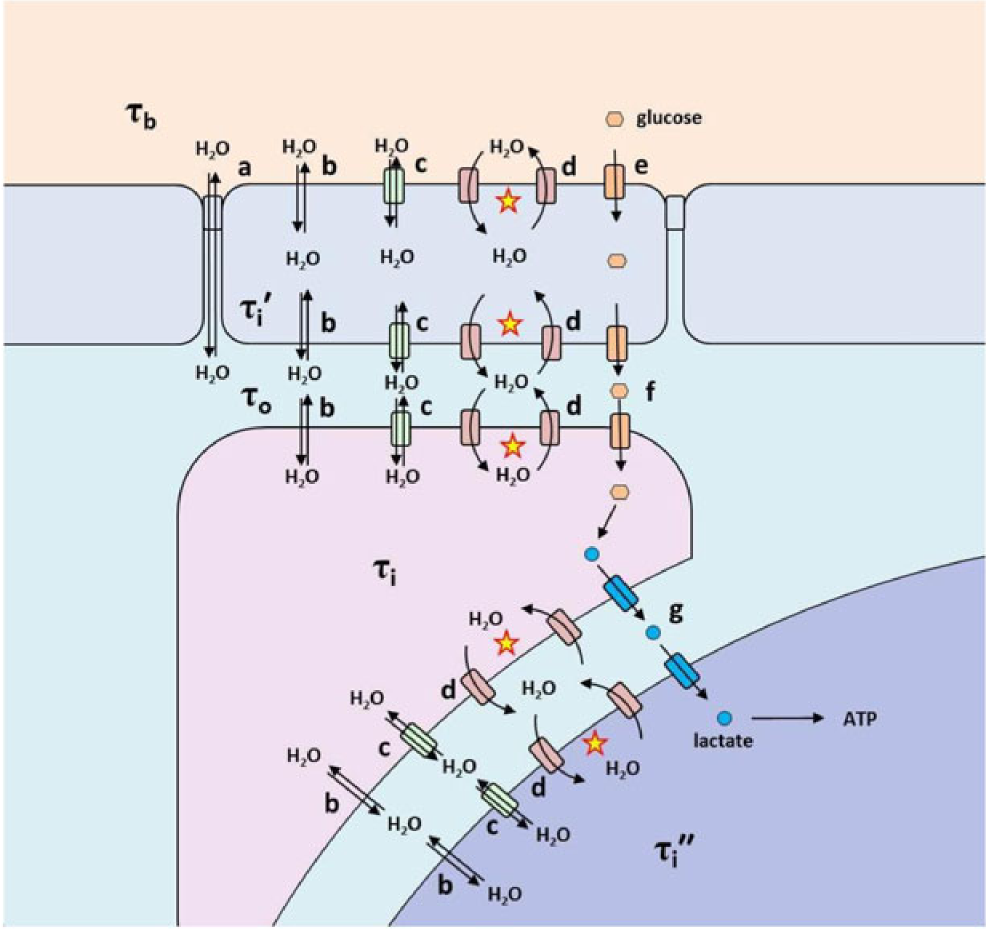

Figure 6. A neurogliovascular unit chain mechanism. Water exchange processes determine mean water molecule lifetimes in blood (τ_b, beige), interstitium (τ_o, aqua), endothelial (τ_i', gray), neuroglial (τ_i, pink), and neuronal (τ_i'', blue) cell spaces. The equilibrium paracellular (a), simple diffusion (b), facilitated transcellular (c), and active water cycling (d, stars) pathways are indicated, as are "Magistretti steps" (e–g). We suggest the d steps couple unit metabolic activity to τ_b.

Table 2. The biomarker k_{po} measures metabolic activity

	SSP DCE-MRI (^1H_2O)		^{31}PMRSI	^{23}NaMRSI	SSP DCE-MRI (^1H_2O)	^{31}PMRSI-MT
	v_b	k_{po} (τ_b^{-1}) (s^{-1})	[ATP$_t$] (mM)	[Na$_t$] (mM)	$k_{po}v_b$ (s^{-1})	CMR$_{oxphos}$ (pmol(ATP) s^{-1} μL^{-1})
Healthy controls						
NWM	0.014	3.2	2.43	19[a]	0.045	50
NGM	0.031	2.9	1.62	31[a]	0.090	160
NGM/NWM					2.0	3.2
Relapsing–remitting MS						
NAWM	0.019	2.2	2.11	27[a]	0.042	
NAGM	0.045	2.0	1.29	36[a]	0.090	
Lesion	0.012	1.8		35[a]	0.022	
Glioblastoma						
NA-frontal WM	0.008	2.6		↑3%[b]	0.021	
NA-thalamus	0.017	2.9		↓12%[b]	0.049	
NA-putamen	0.012	2.5			0.030	
Tumor	0.046	≤0.18		↑51%[b]	≤0.008	
References	this work		78	19, 79	this work	17

[a] Reference 19.
[b] Relative to NWM, Reference 79.

volume. Since $\mathrm{CMR_{oxphos}}$ is an ordinary intensive property (all that is accessible by directly detected ^{31}PMRSI), we must multiply the supra-intensive k_{po} by the intensive v_b in order to compare. Thus, the $k_{po}v_b$ products and the $k_{po}v_b$(NGM)/$k_{po}v_b$(NWM) ratio, 2.0, are displayed in Table 2. The agreement of the flux ratios for these two very different and independent techniques, ^{31}PMRSI-MT and DCE-MRI (^1H_2O), is rather remarkable and strongly suggests k_{po} is proportional to $\mathrm{CMR_{oxphos}}$, *per capillary*.

The Table 2 NGM and NWM [$\mathrm{ATP_t}$] and $\mathrm{CMR_{oxphos}}$ values exemplify the thermodynamics/kinetics distinction. While the steady-state ATP concentration (and thus free energy) per unit tissue volume is 1.5 times greater in NWM than NGM, the oxidative phosphorylation ATP flux in the same unit tissue volume is 3.2 times greater in NGM than NWM.

A neurogliovascular unit chain mechanism

Table 2 shows that k_{po} is proportional to the ATP consumption flux per capillary (the core of the neurogliovascular unit). What could be a mechanism for this? The clue is in a recent report on the heterogeneity, and response to therapy, of cellular τ_i values within human breast tumors *in vivo* (32). That paper also assembles the evidence from model studies that τ_i^{-1} is increased by the gene dosage of, and substrates for, the driving cell membrane P-type ATP-ase ion pump, and decreased by specific inhibitors (33,66). Cellular k_{io} (τ_i^{-1}) reflects P-type ATP-ase turnover, per cell (32). Figure 6(d) visualizes a cascade (or chain) of τ_i changes for cells within the neurogliovascular unit. These are τ_i (neuroglia, pink), τ_i' (endothelial cells), and τ_i'' (neurons, blue). In the Figure 6 diagram, these active processes are indicated by trans-membrane water cycles (stars, 6(d)). The pink cells can be astrocytes, oligodendrocytes, pericytes, etc. (34–37). Combinations of neurons, glia, and microvessels have been termed "gliovascular units" (36), because of their crucial, exquisite symbiotic metabolic and energetic interactions (34,35,37). The Figure 6(d) pathways represent processes driven by NKA turnover, perhaps the most crucial ongoing cellular metabolic activity in the brain. These would affect each other by changes in transporter substrate concentrations ("paracrine communication"). This is plausible because these cells are within synaptic proximities (<50 nm), and have asymmetric transporter distributions. Microjets of water and substrates are continually injected into these confined spaces as transporters turn over. Obligate active trans-membrane water cycling (32) means that water is effectively a substrate for the reactions driven by NKA turnover – the steady-state system for which the forward reaction is given in the Introduction. Thus, it is possible that τ_b in turn reflects ongoing neurogliovascular unit metabolic turnover, particularly $\mathrm{Na^+,K^+}$ATP-ase activity: the smaller τ_b the greater NKA turnover, and vice versa – a cascade of altered active trans-membrane water cycling – a k_{po} decrease reflecting k_{io} decreases within the unit. For example, the "Magistretti mechanism" (Fig. 6(e)–(g)) has neuroglia essentially conducting most glycolysis and transferring lactate to neurons for mostly oxidative phosphorylation: the capillary is intimately involved in this intercellular metabolic cooperativity (34,35). An increase in k_{po} would reflect a speed-up of Magistretti-type processes (Fig. 6(e)–(g)), an exciting hypothesis. The increased k_{po} in NWM (Figs. 2(c) and 3) may reflect increased metabolic activity in common tracts shared by fluctuating resting-state neural circuits. For example, the Figure 2c asymmetry (left centrum semiovale WM hyperintensity (image right)) could reflect a "rich club" node WM connection active at the time of this acquisition (80). Consistent with this, in other subjects (not shown) WM k_{po} hot spot loci vary. The greater spatial resolution planned (see below) could prove informative in this regard. (We note that the BOLD effect reflects the coupling of metabolic activity with vascular properties.) The extravascular water lifetime τ_{exv} is a complicated function of water populations and lifetimes τ_i'', τ_o, τ_i, τ_i', etc. (Fig. 6) (55).

Absolute quantitation

Our results allow calculation of the equilibrium brain capillary water efflux. In 1 μL tissue, we estimated the average capillary length and radius as 2 mm and 2.6 μm, respectively, above. For a cylinder, this gives a mean capillary volume (*V*) of 42.5 pL. A 50 M [H_2O] yields 1.3×10^{15} H_2O molecules per capillary. For NGM, k_{po} is 2.9 $\mathrm{s^{-1}}$ (Table 1). This gives the equilibrium water efflux = $1.3 \times 10^{15} \times 2.9 = 3.8 \times 10^{15}$ H_2O molecules $\mathrm{s^{-1}}$ per capillary (and, of course, an equal influx). Now, consider the homeostatic NGM $\mathrm{CMR_{oxphos}}$, 160 pmol(ATP) $\mathrm{s^{-1}\ \mu L^{-1}}$ (17). If 75% is used for NKA turnover (3), we have 120 pmol(ATP) $\mathrm{s^{-1}\ \mu L^{-1}}$ consumption. For 100 capillaries $\mathrm{\mu L^{-1}}$ (81), this is 1.2 pmol(ATP) $\mathrm{s^{-1}}$ per capillary. The NGM water flux estimated above corresponds to 6 nmol(H_2O) $\mathrm{s^{-1}}$ per capillary, and yields 5×10^3 H_2O molecules cycled per NKA turnover (one ATP molecule consumed). Some individual water co-transporting membrane symporters have H_2O stoichiometries approaching this order of magnitude (69,70,82), and there are likely a number of different symporters involved in the neurogliovascular unit chain (Fig. 6(d)). Thus, in addition to the remarkable agreement with relative $\mathrm{CMR_{oxphos}}$ values in Table 2, it is possible that brain k_{po} values can be interpreted quantitatively. For a 44 μL rat brain ROI *in vivo*, k_{io} was measured as 1.8 $\mathrm{s^{-1}}$ using a very invasive intracerebroventricular CA infusion (83). The chain mechanism (Fig. 6(d)) suggests that k_{po} should be similar to k_{io}.

Clinical implications

This paper does not focus on clinical aspects. However, the approach introduced here has much to offer in this regard.

MS

The longstanding MS imaging hallmark is the "enhancing" WM lesion. In Appendix B, we mention that enhancement (with CA) is transient, and not always "caught" in an MRI study. The Figure 4 late-stage subject is an example. Though her WM lesions are chronic, and large, they were not especially CA-enhancing at the time of acquisition, and their conspicuity in the R_{1exv} map (essentially a T_1-w image inverse) is poor. However, if we inspect the τ_b map (the Fig. 4(c) inverse) in Figure 7, the conspicuity is very high. Thus, the prospect for detecting lesions is much greater with a τ_b map.

Meanwhile, MS understanding is evolving. While long considered a WM disease, emerging data suggest that GM may be an early, or even the initial, disease target (84,85). A recent concept is that MS disease activity originates in brain regions other than WM, perhaps GM; the "outside-in" hypothesis (85). In early disease, pro-inflammatory cytokines are chronically upregulated and can reduce oxygen utilization despite sufficient delivery ("metabolic hypoxia" (86)), mediate mitochondrial function, and decrease neurogenesis, and may increase overall neurodegeneration risk. Metabolic deficits of MS-NAGM are more extensive than those in MS-NAWM and include decreased oxygen

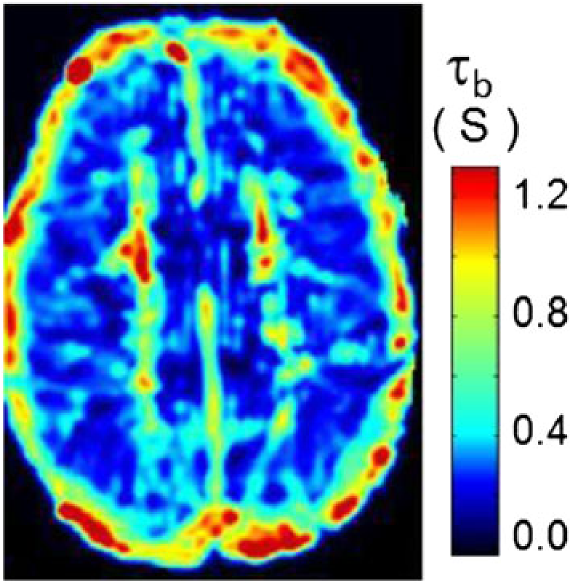

Figure 7. Late-stage MS τ_b map. The τ_b map for the 52 year old female advanced RRMS subject in Fig. 4. This is the Fig. 4(c) k_{po} map inverse. The τ_b values are strongly elevated in lesion areas, and strongly reduced in cortical regions, giving these chronic lesions very high conspicuity. Lesion CA-enhancement (not shown) is almost non-existent. Elevated subarachnoid τ_b values are artifactual.

utilization (85), altered perfusion, and high-energy phosphate depletion (78).

If MS-NAGM and MS-NAWM NKA turnover is diminished by metabolic hypoxia then, according to our mechanism, the supra-intensive k_{po} will decrease. This is what we see (Table 2). The fact that, in RRMS, k_{po} decreases by the same amount (31%) from both NWM and NGM is strong evidence for whole brain involvement. Furthermore, our results predict this should not be detectable by ^{31}PMRSI-MT, which can access only the intensive CMR$_{oxphos}$. Table 2 indicates that $k_{po}v_b$ – the CMR$_{oxphos}$ analog – does not decrease in RRMS NAGM or NAWM: the recruited $\rho^{\dagger}$ increase exactly compensates the $P_W{}^{\dagger}$ decrease.

The TSC is the volume fraction-weighted average of the (extra- and intra-cellular) compartmental Na$^+$ concentrations within the voxel or ROI: $[Na_t{}^+] = v_e[Na_o{}^+] + v_i[Na_i{}^+]$; where $v_e + v_i = 1$. Globally in the brain, v_e is usually thought to be near 0.2 (thus $v_i = 0.8$); $[Na_o{}^+]$ is considered (highly regulated) near 140 mM; and $[Na_i{}^+]$ near 12 mM in normal homeostasis (79). Thus, there are (at least) two general mechanisms for increasing $[Na_t{}^+]$. The first (anatomic) is a v_e increase (with concomitant v_i decrease; cell shrinking; cell density decrease) without changing $[Na_o{}^+]$ or $[Na_i{}^+]$. This is often called the Hilal mechanism. The second (metabolic) is an $[Na_i{}^+]$ increase due to a slow-down of membrane NKA turnover without changing v_e, v_i, or $[Na_o{}^+]$. NKA activity can be regulated in several different ways (3). Of course, there are various possible combinations of the first and second mechanisms simultaneously. The opposite changes could decrease $[Na_t{}^+]$. The good (negative) correlation of k_{po} with $[Na_t{}^+]$ in both normal and NA-MS brain (Table 2) is suggestive of the second mechanism. However, since we do not have an independent measure of v_e (and thus v_i), its interpretation remains ambiguous.

Also exciting is the significantly *increased* MS-NAGM k_{po} in the late-stage disease (Fig. 4(c)). If this is borne out in more subjects, it means that neurogliovascular unit NKA activity is *increased* in advanced MS-NAGM – a strong indication of global metabolic GM involvement, possibly indicating an RRMS to secondary-progressing MS conversion. Access to a metabolic imaging biomarker for this stage change would be of tremendous benefit. Inspection of the same map (Fig. 4(c)) suggests that the demyelinated lesions in WM have greatly diminished resting-state metabolic activity. Perhaps the NAGM activity is increased because of the necessity to employ “detour” circuitry because of blocked rich club node connections. Alternatively, perhaps neurogliovascular unit cells enter apoptosis in advanced MS disease. There is an interesting report that cells intentionally put into a defined apoptotic state exhibit a substantially *increased* k_{io} (87).

GBM tumor

In GBM tumors, k_{po} values less than 1 s^{-1} (Table 2) suggest that NKA turnover is exceptionally slow. This is consistent with tumor $[Na_t]$ being increased by 51% over its value in NWM (79) (Table 2). Our finding that k_{po} values in GBM-NA tissue are similar to those in control brain is also consistent with the fact that tumor-NA tissue $[Na_t]$ values differ little from controls (79) (Table 2). A recent qualitative ^{31}PMRSI investigation of human GBM *in vivo* suggests that $[ATP_t]$ and $[PCr_t]$ values are essentially the same in tumor tissue as in control brain (88). Also it has been found that, while MR$_{glc}$ is only slightly elevated over adjacent WM in GBM tumor (27), there is extensive hypoxia (89). In this condition, ATP production shifts from oxidative phosphorylation toward glycolysis. Within the neurogliovascular unit, this means that the *locus* of ATP synthesis shifts from neurons toward neuroglial cells (34,35). The consequence of this could be that a decrease in neuronal glucose consumption is slightly overcompensated by an increase in neuroglia, which also have proliferated in the tumor. However, net NKA turnover in the neurogliovascular unit, dominated by neurons, would decrease and consequently neuronal $[Na_i]$ would increase. The substantial GBM tumor k_{po} decrease (Table 2) may be a hypoxia signature. Unlike ^{18}FDG PET or gluco-CEST/CESL, the activity we ostensibly measure is catabolically downstream of an oxidative phosphorylation → glycolysis shift. The turnover of NKA is a major end-point of central (intermediary) metabolism.

The population-averaged value of 0.18 s^{-1} for k_{po} in GBM tissue (Table 1) is quite surprisingly small. We find the tumor k_{io} value is substantial in the epithelial cancers (>2.0 s^{-1}, breast carcinoma (32); >2.5 s^{-1}, prostate adenocarcinoma (90)) we have examined (hot spots even larger). Perhaps k_{io} within the GBM tumor is also significant and the small k_{po} really reflects a breakdown of neurogliovascular unit k_{io}/k_{po} coupling. Preliminary analyses of Gd(III) CA DCE-MRI time-courses (not shown) suggest that the GBM tumor k_{io} values are not as small as k_{po}. Of course, the GBM tumor could also have just a decreased metabolic activity.

Stroke

The acute and significant cerebral water apparent diffusion coefficient (ADC) drop after an ischemic event is of considerable clinical importance, though the mechanism has remained elusive. We have suggested (33) that an active trans-membrane water cycling decrease may contribute. Consistent with this, the ADC drops by 40% within 15 min of direct application of ouabain (a specific NKA inhibitor) to the striatum – before there is significant decrease of the NKA substrate ATP$_i$ (91).

Concluding remarks

We have designed a new acquisition pulse sequence that incorporates the "multiband" approach (92,93) and yields full brain coverage with nominal voxel volume less than half that in Figures 2, 4, and 7.

The existence of, or dominance of, an active cell membrane k_{io} has implications for many different types of *in vivo* MR experiment. In the metabo-CEST experiment, The RF-induced ^1H_2O intensity change depends on two factors: (1) the metabolite concentration, and (2) the probability per unit time of a water molecule encountering the metabolite molecule. Some water must cross a cell membrane to gain this access, and we have suggested (61) that this transport can contribute to the metabo-CEST signal. In gluco-CEST, for example, the contribution from intracellular glucose is "very small to negligible" (94). However, about 80% of water is intracellular. An aim of gluco-CEST is to determine relative glucose concentrations (23). Since k_{io} likely changes during a glucose challenge, the probability of intra- and extracellular H_2O molecules crossing the membrane changes. The fact that this would also alter the temporal probability of water encountering glucose could affect the interpretation of gluco-CEST changes. This phenomenon may have already been manifest in the gluco-CESL experiment (24).

It is possible that water movement in living tissue is dominated by active trans-membrane water cycling. Significant shutter-speed effects are very common in cancer MRI (32). (Since the angiogenic microvessels of malignant tumors have larger intrinsic K^{trans} values than benign tumors, the use of SSP DCE-MRI makes it possible to contemplate eliminating most, if not all, unnecessary biopsies (i.e. those that find no malignancy) in breast (95–97) and prostate (31,90) cancer. These comprise about 70% of all breast and prostate biopsies. The K^{trans} values of malignant tumors are systematically suppressed by the TP.) These effects are now also being found in animal and human myocardium *in vivo* (66,68). The NMR shutter-speed concept has broad application.

Acknowledgements

We are grateful for NIH (RO1 NS40801; RO1 EB007258; UO1 CA154602; R44 CA180425; S10 RR027694, and UL1 RR024140) and NMSS (RG 3168A1) support. We appreciate stimulating discussions with Drs Jeffrey Iliff, Craig Jahr, Damien Fair, Kenneth Krohn, Christopher Kroenke, Martin Pike, Wei Huang, Thomas Barbara, Michael Garwood, and Kâmil Uğurbil, as well as the indispensable technical assistance of Mr Brendan Moloney.

REFERENCES

1. Bublitz M, Morth JP, Nissen P. P-type ATPases at a glance. J. Cell Sci. 2011; 124: 2515–2519.
2. Morth JP, Pedersen BP, Buch-Pedersen MJ, Anderson JP, Vilsen B, Palmgren MG, Nissen P. A structural overview of the plasma membrane Na^+,K^+-ATPase and H^+-ATPase ion pumps. Nat. Rev. Mol. Cell Biol. 2011; 12: 60–70.
3. Reinhard L, Tidow H, Clausen MJ, Nissen P. Na^+,K^+-ATPase as a docking station: protein–protein complexes of the Na^+,K^+-ATPase. Cell. Mol. Life Sci. 2013; 70: 205–222.
4. Kutchai H, Geddis LM. Inhibition of the Na,K-ATPase of canine renal medulla by several local anesthetics. Pharmacol. Res. 2001; 43: 399–403.
5. Goldin SM. Active transport of sodium and potassium ions by the sodium and potassium ion-activated adenosine triphosphatase from renal medulla. J. Biol. Chem. 1977; 252: 5630–5642.
6. Han F, Tucker AL, Lingrel JB, Despa S, Bers DM. Extracellular potassium dependence of the Na^+-K^+-ATPase in cardiac myocytes: isoform specificity and effect on phospholemman. Am. J. Cell Physiol. 2009; 297: C699–C705.
7. Wang W, Gao J, Entcheva E, Cohen IS, Gordon C, Mathias RT. A transmural gradient in the cardiac Na/K pump generates a transmural gradient in Na/Ca exchange. J. Membr. Biol. 2010; 233: 51–62.
8. McCall D. Cation exchange and glycoside binding in cultured rat heart cells. Am. J. Physiol. 1979; 236: C87–C95.
9. Garcia A, Fry NA, Karimi K, Liu C-C, Apell H-J, Rasmussen HH, Clarke RJ. Extracellular allosteric Na^+ binding to the Na^+,K^+-ATPase in cardiac myocytes. Biophys. J. 2013; 105: 2695–2705.
10. Jansen MA, Shen H, Zhang L, Wolkowicz PE, Balschi JA. Energy requirements for the Na^+ gradient in the oxygenated isolated heart: effect of changing the free energy of ATP hydrolysis. Am. J. Physiol. Heart Circ. Physiol. 2003; 285: H2437–H2445.
11. Kypriyanov VV, Stewart LC, Xiang B, Kwak J, Deslauriers R. Pathways of Rb^+ influx and their relation to intracellular [Na^+] in the perfused rat heart. Circ. Res. 1995; 76: 839–851.
12. Eisner DA, Smith TW. The Na–K pump and its effectors in cardiac muscle. In *The Heart and Cardiovascular System* (2nd edn), Fozzard HA, Haber E, Jennings RB, Katz AM (eds). Raven: New York, 1992, Chap. 35, pp. 863–902.
13. Vallabhajosula S, Solnes L, Vallabhajosula B. A broad overview of positron emission tomography radiopharmaceuticals and clinical applications: what is new? Semin. Nucl. Med. 2011; 41: 246–264.
14. Brindle K. Watching tumors gasp and die with MRI: the promise of hyperpolarized ^{13}C MR spectroscopic imaging. Br. J. Radiol. 2012; 85: 697–708.
15. Nelson SJ, Kurhanewicz J, Vigneron DB, Larson PEZ, Harzstark AL, Ferrone M, Van Criekinge M, Chang JW, Bok R, Park I, Reed G, Carvajal L, Small EJ, Munster P, Weinberg VK, Ardenkjaer-Larsen JH, Chen AP, Hurd RE, Odegardstuen L-I, Robb FJ, Tropp J, Murray JA. Metabolic imaging of patients with prostate cancer using hyperpolarized [1-^{13}C]pyruvate. Sci. Trans. Med. 2013; 5: 198ra108. DOI: 10.1126/scitranslmed3006070
16. Khalil MM, Tremoleda JL, Bayomy TB, Gsell W. Molecular SPECT imaging: an overview. Int. J. Mol. Imaging 2011. DOI: 10.1155/2011/796025
17. Zhu X-H, Qiao H, Du F, Xiong Q, Liu X, Zhang X, Ugurbil K, Chen W. Quantitative imaging of energy expenditure in human brain. Neuroimage 2012; 60: 2107–2117.
18. Veech RL, Kashiwaya Y, Gates DN, King MT, Clarke K. The energetics of ion distribution: the origin of the resting electric potential of cells. Life 2002; 54: 241–252.
19. Inglese M, Madelin G, Oesingmann N, Babb JS, Wu W, Stoekel B, Herbert J, Johnson G. Brain tissue sodium concentration in multiple sclerosis: a sodium imaging study at 3 Tesla. Brain 2010; 133: 847–857.
20. Haddadin IS, McIntosh A, Meisamy S, Corum C, Styczynski Snyder AL, Powell NJ, Nelson MT, Yee D, Garwood M, Bolan PJ. Metabolite quantification and high-field MRS in breast cancer. NMR Biomed. 2009; 22: 65–76.
21. De Leon-Rodriguez LM, Lubag AJM, Malloy CR, Martinez GV, Gillies RJ, Sherry AD. Responsive MRI agents for sensing metabolism in vivo. Acc. Chem. Res. 2009; 42: 948–957.
22. Haris M, Singh A, Cai K, Kogan F, McGarvey J, DeBrosse C, Zsido GA, Witschey WRT, Koomalsingh K, Pilla JJ, Chirinos JA, Ferrari VA, Gorman JH, Hariharan H, Gorman RC, Reddy R. A technique for *in vivo* mapping of myocardial creatine kinase metabolism. Nat. Med. 2014; 20: 209–214.
23. Walker-Samuel S, Ramasawmy R, Torrealdea F, Rega M, Rajkumar V, Johnson SP, Richardson S, Gonçalves M, Parkes HG, Årstad E, Thomas DL, Pedley RB, Lythgoe MF, Golay X. *In vivo* imaging of glucose uptake and metabolism in tumors. Nat. Med. 2013; 19: 1067–1072.
24. Jin T, Mehrens H, Hendrich KS, Kim S-G. Mapping brain glucose uptake with chemical exchange-sensitive spin-lock magnetic resonance imaging. J. Cereb. Blood Flow Metab. 2014; 34: 1402–1410. DOI: 10.1038/jcbfm2014.97
25. Logan J, Volkow ND, Fowler JS, Wang G-J, Fischman MW, Foltin RW, Abumrad NN, Vitkun S, Gatley SJ, Pappas N, Hitzemann R, Shea CE. Concentration and occupancy of dopamine transporters in cocaine abusers with [^{11}C]cocaine and PET. Synapse 1997; 27: 347–356.

26. Krohn KA. The physical chemistry of ligand–receptor binding identifies some limitations to the analysis of receptor images. Nucl. Med. Biol. 2001; 28: 477–483.
27. Krohn KA, Mankoff DA, Muzi M, Link JM, Spence AM. True tracers: comparing FDG with glucose and FLT with thymidine. Nucl. Med. Biol. 2005; 32: 663–671.
28. Krohn KA, Link JM. Interpreting enzyme and receptor kinetics: keeping it simple, but not too simple. Nucl. Med. Biol. 2003; 30: 819–826.
29. From AHL, Ugurbil K. Standard magnetic resonance-based measurements of the $P_i \rightarrow$ ATP rate do not index the rate of oxidative phosphorylation in cardiac and skeletal muscles. Am. J. Physiol. Cell Physiol. 2011; 301: C1–C11.
30. Balaban RS, Koretsky AP. Interpretation of ^{31}P NMR saturation transfer experiments: what you can't see might confuse you. Am. J. Physiol. Cell Physiol. 2011; 301: C12–C15.
31. Li X, Priest RA, Woodward WJ, Siddiqui F, Beer TM, Garzotto MG, Rooney WD, Springer CS. Cell membrane water exchange effects in prostate DCE-MRI. J. Magn. Reson. 2012; 218: 77–85. DOI: 10.1016/j.jmr.2012.03.019
32. Springer CS, Li X, Tudorica LA, Oh KY, Roy N, Chui SY-C, Naik AM, Holtorf ML, Afzal A, Rooney WD, Huang W. Intra-tumor mapping of intra-cellular water lifetime: metabolic images of breast cancer? NMR Biomed. 2014; 27: 760–773. [DOI: 10.1002/nbm.3111]
33. Zhang Y, Poirier-Quinot M, Springer CS, Balschi JA. Active trans-plasma membrane water cycling in yeast is revealed by NMR. Biophys. J. 2011; 101: 2833–2842. DOI: 10.1016/j.bpj.2011.10.035
34. Lee Y, Morrison BM, Li Y, Lengacher S, Farah MH, Hoffman PN, Liu Y, Tsingalia A, Jin L, Zhang P-W, Pellerin L, Magistretti PJ, Rothstein JD. Oligodendroglia metabolically support axons and contribute to neurodegeneration. Nature 2012; 487: 443–448.
35. Rinholm JE, Bergersen LH. The wrap that feeds neurons. Nature 2012; 487: 435–436.
36. Abbot NJ, Rönnbäck L, Hansson E. Astrocyte–endothelial interactions at the blood–brain barrier. Nat. Rev. Neurosci. 2006; 7: 41–53.
37. Harris JJ, Jolivet R, Attwell D. Synaptic energy use and supply. Neuron 2012; 75: 762–777.
38. Itoh Y, Suzuki N. Control of brain capillary blood flow. J. Cereb. Blood Flow Metab. 2012; 32: 1167–1176.
39. Gesztelyi G, Finnegan W, DeMaro JA, Wang J-Y, Chen J-L, Fenstermacher J. Parenchymal microvascular systems and cerebral atrophy in spontaneously hypertensive rats. Brain Res. 1993; 611: 249–257.
40. Pawlik G, Rackl A, Bing RJ. Quantitative capillary topography and blood flow in the cerebral cortex of cats: an in vivo microscopic study. Brain Res. 1981; 208: 35–58.
41. Hutchinson EB, Stefanovic B, Koretsky AP, Silva AC. Spatial flow-volume dissociation of the cerebral microcirculatory response to mild hypercapnia. Neuroimage 2006; 32: 520–530.
42. Wilson GJ, Woods M, Springer CS, Bastawrous S, Bhargava P, Maki JH. Human whole blood ^1H_2O longitudinal relaxation with normal and high-relaxivity contrast reagents: influence of trans-cell-membrane water exchange. Magn. Reson. Med. 2014; 72: 1746–1754. DOI: 10.1002/mrm.25064
43. Li X, Huang W, Morris EA, Tudorica LA, Seshan VE, Rooney WD, Tagge I, Wang Y, Xu J, and Springer CS. Dynamic NMR effects in breast cancer dynamic-contrast-enhanced MRI. Proc. Natl. Acad. Sci. U. S. A. 2008; 105: 17937–17942.
44. Hills BP, Belton PS. NMR studies of membrane transport. Ann. Rep. NMR Spectrosc. 1989; 21: 99–159.
45. Herbst MD, Goldstein JH. A review of water diffusion measurement by NMR in human red blood cells. Am. J. Physiol. 1989; 256 (Cell Physiol. 25): C1097–C1104.
46. Marshall AG. *Biophysical Chemistry: Principles, Techniques, and Applications*. Wiley: New York, 1978, p. 152.
47. Huang W, Li X, Morris EA, Tudorica LA, Seshan VE, Wang Y, Xu J, Springer CS. The magnetic resonance shutter-speed discriminates vascular properties of malignant and benign breast tumors. Proc. Natl. Acad. Sci. U. S. A. 2008; 105: 17943–17948.
48. Chen S-T, Springer CS. Ionophore-catalyzed cation transport between phospholipid inverted micelles manifest in DNMR. Biophys. Chem. 1981; 14: 375–388.
49. Labadie C, Lee J-H, Vétek G, Springer CS. Relaxographic imaging. J. Magn. Reson. B 1994; 105: 99–112.
50. Eichling JO, Raichle ME, Grubb RL, Ter-Pogossian MM. Evidence of the limitations of water as a freely diffusible tracer in brain of the rhesus monkey. Circ. Res. 1974; 35: 358–364.
51. Paulson OB, Hertz MM, Bolwig TG, Lassen NA. Filtration and diffusion of water across the blood–brain barrier in man. Microvasc. Res. 1977; 13: 113–124.
52. Reid AC, Teasdale GM, McCulloch J. The effects of dexamethasone administration and withdrawal on water permeability across the blood–brain barrier. Ann. Neurol. 1983; 13: 28–31.
53. Silva MD, Helmer KG, Lee J-H, Han SS, Springer CS, Sotak CH. Deconvolution of compartmental water diffusion coefficients in yeast-cell suspensions using combined T_1 and diffusion measurements. J. Magn. Reson. 2002; 156: 52–63.
54. Landis CS, Li X, Telang FW, Molina PE, Pályka I, Vétek G, Springer CS. Equilibrium transcytolemmal water-exchange kinetics in skeletal muscle *in vivo*. Magn. Reson. Med. 1999; 42: 467–478.
55. Li X, Rooney WD, Springer CS. A unified MRI pharmacokinetic theory for intravascular and extracellular contrast reagents. Magn. Reson. Med. 2005; 54: 1351–1359 [Erratum 2006; 55, 1217].
56. Schwarzbauer C, Morrissey SP, Deichmann R, Hillenbrand C, Syha J, Adolf H, Nöth U, Haase A. Quantitative magnetic resonance imaging of capillary water permeability and regional blood volume with an intravascular MR contrast agent. Magn. Reson. Med. 1997; 37: 769–777.
57. Barbier EL, St. Lawrence KS, Grillon E, Koretsky AP, Décorps M. A model of blood–brain barrier permeability to water: accounting for blood inflow and longitudinal relaxation effects. Magn. Reson. Med. 2002; 47: 1100–1109.
58. Rooney WD, Yankeelov TE, Coyle PK, Telang FW, Springer CS. Regional blood volumes and intravascular water lifetimes in human brain. In *Proceedings of the 11th Annual Meeting ISMRM*, international Society for Magnetic Resonance in Medicine, Berkeley, CA: Toronto, Ontario, Canada, 2003, p. 2188.
59. Kim YR, Tejima E, Huang S, Atochin DN, Dai G, Lo EH, Huang PL, Bogdanov A, Rosen BR. *In vivo* quantification of transvascular water exchange during the acute phase of a permanent stroke. Magn. Reson. Med. 2008; 60: 813–821.
60. Huang S, Farrar CT, Dai G, Kwon SJ, Bogdanov AA, Rosen BR, Kim YR. Dynamic monitoring of blood–brain barrier integrity using water exchange index (WEI) during mannitol and CO_2 challenges in mouse brain. NMR Biomed. 2013; 26: 376–385.
61. Strijkers GJ, Hak S, Kok MB, Springer CS, Nicolay K. Three-compartment T_1 relaxation model for intracellular paramagnetic contrast agents. Magn. Reson. Med. 2009; 61: 1049–1058.
62. Ye R, Verkman AS. Simultaneous optical measurement of osmotic and diffusional water permeability in cells and liposomes. Biochemistry 1989; 28: 824–829.
63. Kimelberg HK. Water homeostasis in the brain: basic concepts. Neuroscience 2004; 129: 851–860.
64. Amiry-Moghaddam M, Ottersen OP. The molecular basis of water transport in the brain. Nat. Rev. Neurosci. 2003; 4: 991–1001.
65. Li J, Shaikh SA, Enkavi G, Wen P-C, Huang Z, Tajkhorshid E. Transient formation of water-conducting states in membrane transporters. Proc. Natl. Acad. Sci. U. S. A. 2013; 110: 7696–7701. DOI: 10.1073/pnas.1218986110
66. Zhang Y, Balschi JA. Water exchange kinetics in the isolated heart correlate with Na^+/K^+ ATPase activity: potentially high spatiotemporal resolution *in vivo* MR access to cellular metabolic activity. In *Proceedings of the 21st Annual Meeting ISMRM*, international Society for Magnetic Resonance in Medicine, Berkeley, CA: Salt Lake City, UT, USA, 2013, p. 4045.
67. Poirier-Quinot M, He H, Springer CS, Balschi JA. ^1H_2O MR relaxography of the perfused rat heart. In *Proceedings of the 14th Annual Meeting ISMRM*, international Society for Magnetic Resonance in Medicine, Berkeley, CA: Seattle, WA, USA, 2006, p. 1176.
68. Rooney WD, Broberg CS, Springer CS. Tau$_i$, a metabolic imaging biomarker for myocardium. In *Proceedings of the 22nd Annual Meeting ISMRM*, international Society for Magnetic Resonance in Medicine, Berkeley, CA: Milan, Italy, 2014, 2460.
69. Zeuthen T Water-transporting proteins. J. Membr. Biol. 2010; 234: 57–73.
70. Zeuthen T, MacAulay N. Transport of water against its concentration gradient: fact or fiction? WIREs Membr. Transp. Signal. 2012; 1: 373–381.

71. Haase A. Snapshot FLASH MRI. Applications to T1, T2, and chemical-shift imaging. Magn. Reson. Med. 1990; 13: 77–89.
72. Grinstead JW, Rooney WD. Fast T1 mapping in human brain using inversion recovery EPI with GRAPPA at 3T and 7T. In *Proceedings of the 16th Annual Meeting ISMRM*, international Society for Magnetic Resonance in Medicine, Berkeley, CA: Toronto, Ontario, Canada, 2008, p. 3084.
73. Gahramanov S, Raslan AM, Muldoon LI, Hamilton BE, Rooney WD, Várallyay CG, Njus JM, Haluska M, Neuwelt EA. Potential for differentiation of pseudoprogression from true tumor progression with dynamic susceptibility-weighted contrast-enhanced magnetic resonance imaging using ferumoxytol versus gadoteridol: a pilot study. Int. J. Radiat. Oncol. Biol. Phys. 2011; 79: 514–523.
74. Rooney WD, Johnson G, Li X, Cohen ER, Kim S-G, Ugurbil K, Springer CS. Magnetic field and tissue dependences of human brain longitudinal ^1H_2O relaxation *in vivo*. Magn. Reson. Med. 2007; 57: 308–318.
75. Njus JM, Várallyay CS, Grinstead JW, Li X, Springer CS, Neuwelt EA, Rooney WD. DCE-MRI of human brain tumors using Gadoteridol and Ferumoxytol. In *Proceedings of the 16th Annual Meeting ISMRM*, international Society for Magnetic Resonance in Medicine, Berkeley, CA: Toronto, Ontario, Canada, 2008, p. 453.
76. Li X, Springer CS, Jerosch-Herold M. First-pass dynamic contrast-enhanced MRI with extravasating contrast reagent: evidence for human myocardial capillary recruitment in adenosine-induced hyperemia. NMR Biomed. 2009; 22: 148–157. DOI: 10.1002/nbm.1293
77. Nagelhus EA, Ottersen OP. Physiological roles of aquaporin-4 in brain. Physiol. Rev. 2013; 93: 1543–1562.
78. Sammi MK, Berlow Y, Barbara T, Selzer A, Grinstead J, Kim E, Bourdette D, Rooney W. Decreased cellular energetics in multiple sclerosis gray matter: a 7T phosphorus spectroscopy study. Neurology 2012; 78: S21.004.
79. Ouwerkerk R, Bleich KR, Gillen JS, Pomper MG, Bottomley PA. Tissue sodium concentration in human brain tumors as measured with ^{23}Na MR imaging. Radiology 2003; 227: 529–537.
80. Van den Heuvel MP, Sporns O. Rich-club organization of the human connectome. J. Neurosci. 2011; 31: 15775–15786.
81. Cavalia M, Dombrowski SM, Drazba J, Vasanji A, Borkesch PM, Janigro D. Regional variation in brain capillary density and vascular response to ischemia. Brain Res. 2001; 910: 81–93.
82. Marquet P, Depeursinge C, Magistretti PJ. Exploring neural cell dynamics with digital holographic microscopy. Ann. Rev. Biomed. Eng. 2013; 15: 407–431.
83. Quirk JD, Bretthorst GL, Duong TQ, Snyder AZ, Springer CS, Ackerman JJH, Neil, JJ. Equilibrium water exchange between the intra- and extracellular spaces of mammalian brain. Magn. Reson. Med. 2003; 50: 493–499.
84. Miron VE, Kuhlmann T, Antel JP. Cells of the oligodendroglial lineage, myelination, and remyelination. Biochim. Biophys. Acta 2011; 1812: 184–193.
85. Popescu BF, Lucchinetti CF. Meningeal and cortical grey matter pathology in multiple sclerosis. BMC Neurol. 2012; 12: 11. DOI: 10.1186/1471-2377-12-11
86. Ge Y, Zhang Z, Lu H, Tang L, Jaggi H, Herbert J, Babb JS, Rusinek H, Grossman RI. Characterizing brain oxygen metabolism in patients with multiple sclerosis with T_2-relaxation-under-spin-tagging MRI. J. Cereb. Blood Flow Metab. 2012; 32: 403–412.
87. Bailey C, Giles A, Czarnota GJ, Stanisz GJ. Detection of apoptotic cell death *in vitro* in the presence of Gd-DTPA-BMA. Magn. Reson. Med. 2009; 62: 46–55.
88. Ha D-H, Choi S, Oh JY, Yoon SK, Kang MJ, Kim K-U. Application of ^{31}P MR spectroscopy to the brain tumors. Korean J. Radiology 2013; 14: 477–486.
89. Rajendran JG, Mankoff DA, O'Sullivan F, Peterson LM, Schwartz DL, Conrad EU, Spence AM, Muzi M, Farwell DG, Krohn KA. Hypoxia and glucose metabolism in malignant tumors: Evaluation by [^{18}F] fluoromisonidazole and [^{18}F]fluorodeoxyglucose positron emission tomography imaging. Clin. Cancer Res. 2004; 10: 2245–2252.
90. Li X, Priest RA, Woodward WJ, Tagge IJ, Siddiqui F, Huang W, Rooney WD, Beer TM, Garzotto MG, Springer CS. Feasibility of shutter-speed DCE-MRI for improved prostate cancer detection. Magn. Reson. Med. 2013; 69: 171–178. DOI: 10.1002/mrm.24211
91. Veldhuis WB, van der Stelt M, Delmas F, Gillet B, Veldink GA, Vliegenthart JFG, Nicolay K, Bår PR. *In vivo* excitotoxicity induced by ouabain, a Na^+/K^+-ATPase inhibitor. J. Cereb. Blood Flow Metab. 2003; 23: 62–74.
92. Grinstead JW, Wang D, Bhat H, Deshphande V, Cauley SF, Setsompop K, Benner T, Anderson VC, Rooney WD. Slice accelerated inversion recovery T_1 mapping. In *Proceedings of the 22nd Annual Meeting ISMRM*, international Society for Magnetic Resonance in Medicine, Berkeley, CA: Milan, Lombardy, Italy, 2014, p. 3215.
93. Breuer FA, Blaimer M, Heidemann RM, Mueller MF, Griswold MA, Jakob PM. Controlled aliasing in parallel imaging results in higher acceleration (CAIPIRINHA) for multi-slice imaging. Magn. Reson. Med. 2005; 53: 684–691.
94. Chan KWY, McMahon MT, Kato Y, Liu G, Bulte JWM, Bhujwalla ZM, Artemov D, van Zijl PCM. Natural D-glucose as a biodegradable MRI contrast agent for detecting cancer. Magn. Reson. Med. 2012; 68: 1764–1773.
95. Huang W, Tudorica LA, Li X, Thakur SB, Chen Y, Morris EA, Tagge IJ, Korenblit M, Rooney WD, Koutcher JA, Springer CS. Discrimination of benign and malignant breast lesions by using shutter-speed dynamic contrast-enhanced MR imaging. Radiology 2011; 261: 394–403. DOI: 10.1148/radiol.11102413
96. Yankeelov TE, Rooney WD, Huang W, Dyke JP, Li X, Tudorica A, Lee J-H, Koutcher JA, Springer CS. Evidence for shutter-speed variation in CR bolus-tracking studies of human pathology. NMR Biomed. 2005; 18: 173–185.
97. Springer CS, Tudorica LA, Li X, Thakur S, Morris EA, Oh KY, Kettler MD, Chen Y, Tagge IJ, Hemmingson SL, Korenblit M, Grinstead JW, Laub G, Koutcher JA, Huang W. Meta-population breast cancer screening with the ΔK^{trans} DCE-MRI parameter. In *Proceedings of the 19th Annual Meeting ISMRM*, international Society for Magnetic Resonance in Medicine, Berkeley, CA: Montréal, Québec, Canada, 2011, p. 3097.
98. Njus JM, Li X, Springer CS, Taylor M, Greisel T, Telang FW, Coyle PK, Rooney WD. Changes in blood–brain barrier permeability and blood volume during MS lesion development and evolution. In *Proceedings of the 16th Annual Meeting ISMRM*, international Society for Magnetic Resonance in Medicine, Berkeley, CA: Toronto, Ontario, Canada, 2008, p. 3431.
99. Njus JM, Li X, Springer CS, Taylor M, Telang FW, Coyle PK, Rooney WD. DCE-MRI K^{trans} mapping of MS lesion evolution in individuals. In *Proceedings of the 16th Annual Meeting ISMRM*, international Society for Magnetic Resonance in Medicine, Berkeley, CA: Toronto, Ontario, Canada, 2008, p. 3434.
100. Landis CS, Li X, Telang FW, Coderre JA, Micca PL, Rooney WD, Latour LL, Vetek G, Palyka I, Springer CS. Determination of the MRI contrast agent concentration time course in vivo following bolus injection: effect of equilibrium transcytolemmal water exchange. Magn. Reson. Med. 2000; 44: 563–574.

APPENDIX A

k_{po} VARIATIONS AND ACCOMPANYING v_b VARIATIONS

Consider (conservatively) the MS-induced GM k_{po} change – the smallest in Table 1. We have $\langle \tau_b(\mathrm{NAGM}) \rangle^{-1} / \langle \tau_b(\mathrm{NGM}) \rangle^{-1}$ = 2.0 s^{-1}/2.5 s^{-1} = 0.80: the NAGM $\langle \tau_b \rangle^{-1}$ is reduced by 20% from that in NGM ($\langle k_{po} \rangle$ is reduced by 31%). From the fundamental theoretical relationship, $\langle \tau_b(\mathrm{NAGM}) \rangle^{-1} / \langle \tau_b(\mathrm{NGM}) \rangle^{-1} = [P_W^{\dagger}(\mathrm{NAGM})/P_W^{\dagger}(\mathrm{NGM})](r_{NGM}/r_{NAGM})$, where r_{NGM} and r_{NAGM} are the mean capillary radii in NGM and NAGM tissues, respectively. (Capillaries dominate vascular volume in most voxels (39,41).) Thus, the experimental relationship $[P_W^{\dagger}(\mathrm{NAGM})/P_W^{\dagger}(\mathrm{NGM})](r_{NGM}/r_{NAGM}) = 0.80$ must be satisfied. There is an infinite number of possibilities: if $r_{NAGM} = 1.25 r_{NGM}$, $P_W^{\dagger}(\mathrm{NAGM}) = P_W^{\dagger}(\mathrm{NGM})$; if $r_{NAGM} = r_{NGM}$, $P_W^{\dagger}(\mathrm{NAGM}) = 0.8 P_W^{\dagger}(\mathrm{NGM})$; etc.

It is extremely difficult, and invasive, to determine individual capillary radii *in vivo* (38,40,41). However, we can estimate capillary radius changes, if any, from our data. The blood volume fraction $v_b = (n/V_T)V = \rho^{\dagger}V$, where n/V_T is the number of

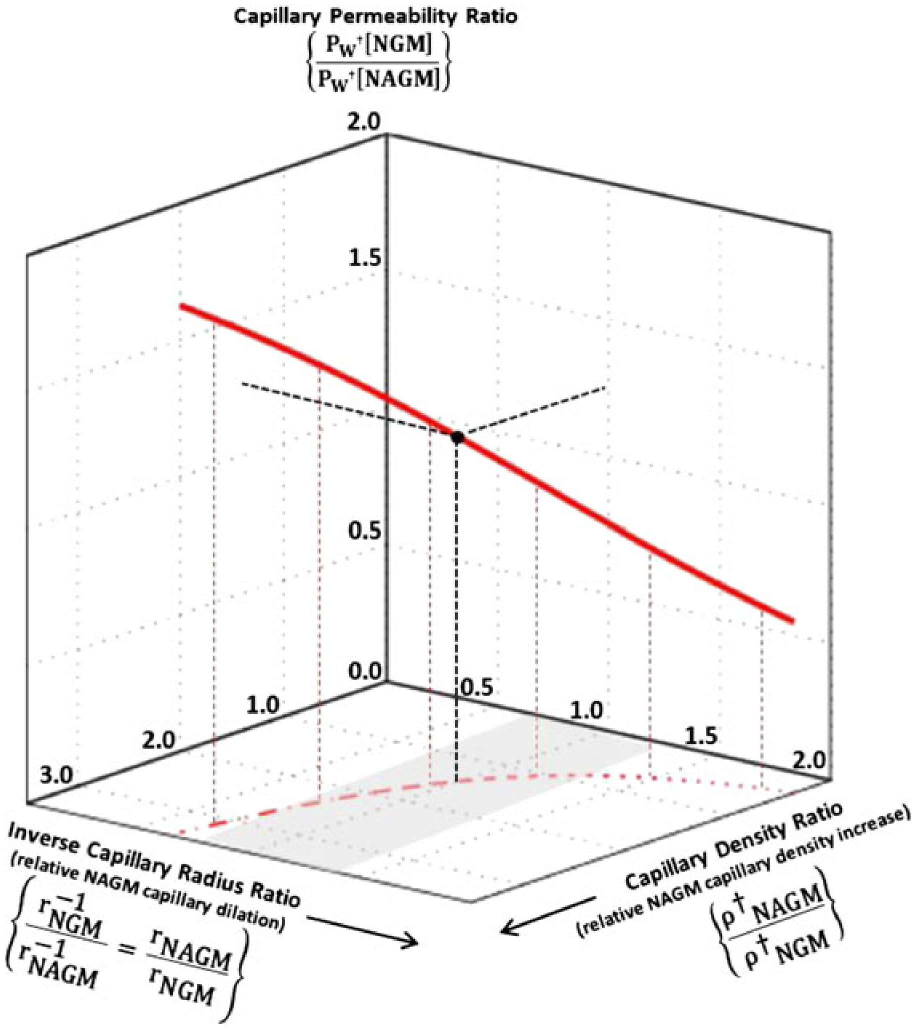

Figure A1. Capillary property space. A plot of biomarker inter-relationships for population-averaged NGM and NAGM ROI values in Table 1. Thus, $\langle\tau_b(\mathrm{NAGM})\rangle^{-1}/\langle\tau_b(\mathrm{NGM})\rangle^{-1} = 0.80$, and $v_b(\mathrm{NAGM})/v_b(\mathrm{NGM}) = 1.5$, where $\tau_b^{-1} \equiv k_{po}$ (τ_b is the mean capillary water lifetime) and v_b the capillary volume fraction. The red curve is the trace of points that satisfy these experimental relationships simultaneously, in a 3D space of brain tissue microvascular properties. The vertical axis is $P^{\dagger}_W(\mathrm{NGM})/P^{\dagger}_W(\mathrm{NAGM})$, the capillary water permeability coefficient ratio. The oblique axes are the inverse capillary radius ratio, $r^{-1}_{\mathrm{NGM}}/r^{-1}_{\mathrm{NAGM}}$ ($=r_{\mathrm{NAGM}}/r_{\mathrm{NGM}}$), and the capillary density ratio, $\rho^{\dagger}_{\mathrm{NAGM}}/\rho^{\dagger}_{\mathrm{NGM}}$. The coordinates of the curve in regions of reasonable $r_{\mathrm{NAGM}}/r_{\mathrm{NGM}}$ (gray shading) are consistent only with τ_b being dominated by the $P_W{}^{\dagger}$ factor. When $r_{\mathrm{NAGM}} = r_{\mathrm{NGM}}$ (black point), $\rho^{\dagger}_{\mathrm{NAGM}} = 1.44\rho^{\dagger}_{\mathrm{NGM}}$, and $P_W{}^{\dagger}(\mathrm{NGM}) = 1.25P^{\dagger}_W(\mathrm{NAGM})$. $P_W{}^{\dagger}$ is reduced in resting-state NAGM from its value in resting-state NGM.

capillaries in the voxel or ROI total volume, the capillary number density, $\rho^{\dagger}$ (hundreds $\mu\mathrm{L}^{-1}$ (81)), and V is the mean individual capillary volume. Assuming cylindrical capillaries, $r \sim V^{1/2}$ and the ratio $[v_b(\mathrm{NGM})/v_b(\mathrm{NAGM})]^{1/2} = (\rho^{\dagger}_{\mathrm{NGM}}/\rho^{\dagger}_{\mathrm{NAGM}})^{1/2}(r_{\mathrm{NGM}}/r_{\mathrm{NAGM}})$. Taking $v_b(\mathrm{NGM})$ as 0.031 and $v_b(\mathrm{NAGM})$ as 0.045 (Table 1) gives $[v_b(\mathrm{NGM})/v_b(\mathrm{NAGM})]^{1/2} = 0.83$.

The solid red curve in Figure A1 is the trace of all points that simultaneously satisfy the experimental relationships $[P_W{}^{\dagger}(\mathrm{NAGM})/P_W{}^{\dagger}(\mathrm{NGM})](r_{\mathrm{NGM}}/r_{\mathrm{NAGM}}) = 0.80$ and $(\rho^{\dagger}_{\mathrm{NGM}}/\rho^{\dagger}_{\mathrm{NAGM}})^{1/2}(r_{\mathrm{NGM}}/r_{\mathrm{NAGM}}) = 0.83$ (from the population- and ROI-averaged Table 1 biomarker values), in a 3D space of tissue microvascular properties. The axes are $P_W{}^{\dagger}(\mathrm{NGM})/P_W{}^{\dagger}(\mathrm{NAGM})$ (vertical), $r^{-1}_{\mathrm{NGM}}/r^{-1}_{\mathrm{NAGM}}$ (inverse capillary radius ratio, $=r_{\mathrm{NAGM}}/r_{\mathrm{NGM}}$), and $\rho^{\dagger}_{\mathrm{NAGM}}/\rho^{\dagger}_{\mathrm{NGM}}$ (capillary density ratio). This is very informative. The dot–dashed red projection does not pass through the $r_{\mathrm{NGM}} = r_{\mathrm{NAGM}}$, $\rho^{\dagger}_{\mathrm{NGM}} = \rho^{\dagger}_{\mathrm{NAGM}}$ point. The experimental data are incompatible with the mean capillary radius and density simultaneously remaining invariant from NGM to NAGM. The brain literature generally indicates it is more likely that chronic v_b differences are due to capillary density ($\rho^{\dagger}$) differences than to capillary dilation or constriction (r changes) (38–41). (Even in an acute hypercapnic perturbation, the microvascular radii for the dominant capillary volume fraction remain unchanged (41). The very smallest capillaries, normally effectively occluded, are opened during the hypercapnia – there is some "recruitment" – but in most capillaries there is a blood velocity increase (41).) When the (solid) red curve passes through $r_{\mathrm{NAGM}} = r_{\mathrm{NGM}}$ (black point), the other coordinates are $\rho^{\dagger}_{\mathrm{NAGM}} = 1.44\,\rho^{\dagger}_{\mathrm{NGM}}$ and $P_W{}^{\dagger}(\mathrm{NGM}) = 1.25\,P_W{}^{\dagger}(\mathrm{NAGM})$ (dashed black lines). A conservatively large area for r_{NAGM} from 0.75 r_{NGM} to 1.25 r_{NGM} is shaded gray in the Figure A1 bottom plane. Over this area, the red curve $\rho^{\dagger}_{\mathrm{NAGM}}$ coordinates range from 2.56 $\rho^{\dagger}_{\mathrm{NGM}}$ to 0.92 $\rho^{\dagger}_{\mathrm{NGM}}$, and the $P^{\dagger}_W(\mathrm{NGM})$ coordinates range from 1.67 $P^{\dagger}_W(\mathrm{NAGM})$ to 1.0 $P^{\dagger}_W(\mathrm{NAGM})$. These results clearly indicate that the mean capillary water permeability in MS NAGM is reduced from its value in NGM. For equal mean capillary radii, $P^{\dagger}_W(\mathrm{NAGM}) = 0.8P^{\dagger}_W(\mathrm{NGM})$, $P^{\dagger}_W$ is reduced by 20%. Recall that r is the average for a large number of capillaries. Only 100 capillaries $\mu\mathrm{L}^{-1}$ means 4000 per 40 μL voxel. The Table 1 ROIs represent 80–100 voxels.

100 voxel ROIs in six subjects yield averages over 2 400 000 capillaries. The analogous exercise indicates an even greater $P_W^\dagger$ decrease in MS-NAWM. k_{po} (τ_b^{-1}) is dominated by the $P_W^\dagger$ factor, not the r^{-1} factor.

For the GBM tumor, we make the same analysis, using tissue ROI- and population-averaged parameter values from Table 1. There is a 93% decrease in tumor (T) k_{po} relative to putamen (P). If the permeability coefficients were equal ($P_W{}^\dagger(T) = P_W{}^\dagger(P)$), then $r_T = 14r_P$ (with r_T and r_P the mean capillary radii in tumor and putamen tissue, respectively). It is even more unlikely than in the MS-NAGM tissue that capillaries would dilate by more than an order of magnitude in the tumor tissue. As above, the ratio $[v_b(P)/v_b(T)]^{1/2} = (\rho_P{}^\dagger/\rho_T{}^\dagger)^{1/2}(r_P/r_T)$. Unlike the MS lesions (Table 1), however, the tumor $v_b(T)$, 0.046, is increased over normal-appearing tissue, $v_b(P) = 0.012$. (This reinforces that k_{po} is indeed independent of v_b. It is decreased in MS lesions and in GBM tumors, though v_b is decreased in the former and increased in the latter.) This gives $[v_b(P)/v_b(T)]^{1/2} = 0.51$. Though extremely unlikely, if r_T were actually $14r_P$, then $\rho_T{}^\dagger = 0.020\rho_P{}^\dagger$: the tumor capillary density would be less than 3% of that of normal brain – even more unreasonable. An unchanged $P_W^\dagger$ value is incompatible with both the k_{po} and v_b changes. If $r_T = r_P$, then $\rho_T{}^\dagger = 3.8\rho_P{}^\dagger$, and capillary density is increased almost fourfold in the tumor. This is plausible, and explains the v_b ratio. (However, capillary density does not affect the supra-intensive $P_W{}^\dagger$ value.) If $r_T = r_P$, $P_W{}^\dagger(T) = 0.072P_W{}^\dagger(P)$. Whatever the actual capillary radius change, if any, it seems certain that overall $P_W{}^\dagger$ is much *decreased* in the tumor.

APPENDIX B

CALCULATION OF CAPILLARY TRANS-CELLULAR WATER FLUX

We pursue the significance of decreased MS lesion k_{po} – decreased trans-endothelial water exchange. Consider lesion K^{trans} values. The biomarker $K^{trans} \approx P_{CA}{}^\dagger S$, where $P_{CA}{}^\dagger$ is the endothelial CA permeability coefficient (76). The DCE-MRI enhancement of MS lesions is transient during disease progression, increasing and decreasing with time-constants of months (98,99), making them hard to "catch." When measurable, however, the K^{trans} values exhibit intra-lesion heterogeneity, and can reach magnitudes over 10^{-2} min^{-1} (96,98,99). Thus, active MS lesions exhibit significantly increased K^{trans} values, and these remain elevated above NWM values (10^{-5} min^{-1}) for at least six months after maximum enhancement (98). Though the chronic Figure 4 lesions are no longer "active" in the clinical sense, their K^{trans} values are still ten times normal (98). Since v_b is decreased in the Figure 4 MS lesions, the S quantity must be as well. Thus, $P_{CA}{}^\dagger$ must be significantly increased. There is little doubt that CA employs the para(endothelial)cellular pathway (Fig. 6(a) for capillary extravasation: the endothelial cell junctions must open somewhat (36) in an MS lesion. The paracellular pathway must also constitute a component of the passive *water* permeability, $P_W{}^\dagger$(passive), contribution. Thus, it is highly likely that, in an MS lesion, $P_W{}^\dagger$(passive) is *increased*. However, we see that in the lesion overall $P_W{}^\dagger$ is *decreased* (k_{po} is decreased). The conclusion is that $P_W{}^\dagger$(active) is significantly decreased in an MS lesion.

Also, for monomeric Gd(III) chelate CAs, $P_{CA}{}^\dagger S$ (K^{trans}) is greatly *increased* (four orders of magnitude) in GBM tumors (see Fig. 5, center) (75), mostly due to the $P_{CA}{}^\dagger$ factor (since the v_b increase is less than one order of magnitude). There is little doubt that this is due to widened para(endothelial) cellular pores. Thus, paracellular water extravasation (a $P_W{}^\dagger$(passive) pathway) must also increase. However, this would make k_{po} *increase*. Once again, we are left with the essentially inescapable conclusion that $P_W{}^\dagger$(active) is very much decreased in the brain pathology.

Previously, we calculated the equilibrium brain capillary water efflux in 1 μL tissue for an average capillary length and radius of 2 mm and 2.6 μm, respectively. For a cylinder, this gives a mean capillary volume (V) of 42.5 pL. A 50 M [H_2O] yields 1.3×10^{15} H_2O molecules per capillary. For NGM, k_{po} is 2.9 s^{-1} (Table 1). This gives the equilibrium water efflux = $1.3 \times 10^{15} \times 2.9 = 3.8 \times 10^{15}$ H_2O molecules s^{-1} per capillary (and, of course, an equal influx). Extravasating CA molecules surely use the paracellular pathway (Fig. 6(a); for H_2O). A typical maximum plasma CA concentration is 3 mM (100). The blood $[CA_b]_{max} = (1 - h)[CA_p]_{max}$. A 0.4 hematocrit ($h$) yields $[CA_b]_{max} = 0.6 \times 3 = 1.8$ mM. Thus, at maximum, there are $1.8 \times 10^{-3} \times 42.5 \times 10^{-12} \times 6.0 \times 10^{23} = 4.6 \times 10^{10}$ CA molecules per capillary. The CA extravasation first-order rate constant (k_{pe}) is K^{trans}/v_p (31,32,43,47), also supra-intensive. A large K^{trans} value, 0.1 min^{-1}, say for a GBM tumor capillary, and $v_p = (1 - h)v_b = 0.6 \times 0.03 = 0.02$, yields $k_{pe} = 8.3 \times 10^{-2}$ s^{-1}. This gives a maximum efflux = $4.6 \times 10^{10} \times 8.3 \times 10^{-2} = 3.8 \times 10^{9}$ CA molecules s^{-1} per capillary. Thus the minimal H_2O efflux/CA efflux ratio is 1 000 000. Even if 28 000 H_2O molecules accompanied each CA molecule ($[H_2O]/[CA_b]_{max}$) through the paracellular tight junction pore (Fig. 6(a)), there would be 972 000 H_2O molecules simultaneously exiting by transcellular pathways (Fig. 6(b)–(d)). Only 3% of water employs the paracellular pathway (Fig. 6(a)); 97% of equilibrium water flux is transcellular (Fig. 6(b)–(d)). This is for quite leaky capillaries: less permeable vessels would give an even greater transcellular percentage. (Though the K^{trans} for head muscle tissue is greater, 0.15 min^{-1} (96), k_{po} may be more than 10 s^{-1} (56). Consequently, even in that case less than 1% of the steady-state water flux is paracellular (Fig. 6(a)).) Thus, for the normal brain (K^{trans} ~10^{-5} min^{-1}) by far the vast majority of capillary water efflux occurs via one or more transcellular processes.